# Experimental and theoretical studies of the Xe-OH(A/X) quenching system

J. Kłos,[1, a)] G. McCrudden,[2] M. Brouard,[2, b)] T. Perkins,[2] S. A. Seamons,[2] D. Herráez-Aguilar,[3] and F.J. Aoiz[4, c)]

[1)] *Department of Chemistry and Biochemistry, University of Maryland, College Park, MD 20742-2021, USA*

[2)] *The Department of Chemistry, University of Oxford, The Chemistry Research Laboratory, 12 Mansfield Road, Oxford, OX1 3TA, United Kingdom.*

[3)] *Departamento de Química Física, Facultad de Química, Universidad Complutense, 28040 Madrid, and Faculty of Experimental Sciences, Francisco de Vitoria University (UFV), 28223 Pozuelo de Alarcón (Madrid), Spain.*

[4)] *Departamento de Química Física, Facultad de Química, Universidad Complutense, 28040 Madrid, Spain.*

(Dated: 18 October 2018)

New multi-reference, global *ab initio* potential energy surfaces are reported for the interaction of Xe atoms with OH radicals in their ground $X^2\Pi$ and excited $A^2\Sigma^+$ states, together with the non-adiabatic couplings between them. The $2A'$ excited potential features a very deep well at the collinear Xe–OH configuration whose minimum corresponds to the avoided crossing with the $1A'$ potential energy surface. It is therefore expected that, as with collisions of Kr+OH(A), electronic quenching will play a major role in the dynamics, competing favorably with rotational energy transfer within the $2A'$ state. The surfaces and couplings are used in full three-state surface-hopping trajectory calculations, including roto-electronic couplings, to calculate integral cross-sections for electronic quenching and collisional removal. Experimental cross-sections, measured using Zeeman quantum beat spectroscopy, are also presented here for comparison with these calculations. Unlike similar previous work on the collisions of OH(A) with Kr, the surface-hopping calculations are only able to account qualitatively for the experimentally observed electronic quenching cross-sections, with those calculated being around a factor of two smaller than the experimental ones. However, the predicted total depopulation of the $2A'$ (quenching plus rotational energy transfer) agrees well with the experimental results. Possible reasons for the discrepancies are discussed in detail.



[a)]Electronic mail: jklos@umd.edu

[b)]Electronic mail: mark.brouard@chem.ox.ac.uk

[c)]Electronic mail: aoiz@quim.ucm.es

This manuscript was accepted by J. Chem. Phys. Click here to see the version of record.

## I. INTRODUCTION

Electronically adiabatic and non-adiabatic collisions of the OH($A^2\Sigma^+$) (referred to hereafter as OH(A)) radical have been of considerable interest for a number of years.[1–11] Apart from the relevance of OH to atmospheric chemistry,[12–15] the family of OH(A) + Rg systems (Rg = rare gas) is a widely studied prototype for collisions of an open-shell diatomic radical that is amenable to high-level theory.[2,10,16] In addition, collisions with the heavier rare gases (Kr and Xe) provide an opportunity to study electronic quenching, and its interactions with electronically adiabatic processes, in a simple three-atom system. OH–Xe hydrogen-bonded systems are also of interest in studies of more complex organic molecules that contain the hydroxyl group and which are submerged in an Xe gas matrix. Ildiz *et al.*[17] studied the influence of the Xe matrix on the OH vibrational modes for several organic molecules and calculated interaction energies for a series of complexes containing -OH–Xe bonding.

In contrast to previously studied systems such as OH(A) + He/Ar,[3–7,10] where the crossing between the excited $A^2\Sigma^+$ and ground $X^2\Pi$ potentials is located high on the repulsive wall, the OH(A) + Kr/Xe systems display conical intersections that are accessible at thermal collision energies.[8,11,18] For OH(A) + Kr, there is a region of significant coupling to the ground state close to the most attractive part of the excited-state potential energy surface (PES), in the near-linear HO–Kr configuration,[8] and it is expected that the same or an even more pronounced feature will happen for the OH(A) + Xe system.

This paper presents a set of new PESs for the interaction of xenon with OH($X^2\Pi$) (hereafter, OH(X)) comprising one symmetric $1^2A'$ state and one antisymmetric $1^2A''$ state. A third, excited PES, which correlates asymptotically with OH(A)+Xe, and for which the PES is symmetric under $C_s$ symmetry, $2^2A'$, is also reported. The electrostatic coupling between the diabatic surfaces is also presented here. These form a natural extension of our previous work on the OH(X,A) + Kr system.[8,10,11] In the case of collisions with Xe, the electronic quenching is even more efficient, with cross-sections on the order of $\approx 20\,\text{Å}^2$ as compared with $\approx 8\,\text{Å}^2$ in the collisions with Kr.[1]

These surfaces and couplings will be used for dynamical calculations of integral cross-sections for electronic quenching in OH(A) + Xe, as well as theoretical rotational-state distributions for the quenched OH(X) products, using a recently developed three-state surface-hopping trajectory model that includes roto-electronic couplings.[11] Quenching cross-sections

will also be measured experimentally and compared to the results of these calculations in order to gauge the accuracy of the potentials and dynamical theory presented here.

To our knowledge, the present OH(A) + Xe PES is the first that has been reported in the literature, but PESs for OH(X) + Xe have recently been published by Gilijamse *et al.*[19] That work also reported crossed molecular beam experimental studies of OH(X) + Xe collisions. Collisions with the ground electronic state of OH were also investigated in the 300 K regime by Paterson and coworkers with a focus on angular momentum depolarization.[20,21] Sarma *et al.*[22] also performed joint theoretical and experimental crossed molecular beam studies to generate differential cross-sections for OH(X)+Xe scattering at a collision energy of 483 $cm^{-1}$.

This paper is organized as follows. Section II presents the details of the *ab initio* calculations and describes the main features of the PESs and couplings. The methods for dynamical calculations and experimental measurements of cross-sections are then set out in Section III. After this, Section IV compares experimental and theoretical results for electronic quenching and the state distributions of quenched OH(X) products, and the paper is concluded in Section V.

## II. *AB INITIO* CALCULATIONS

To perform scattering calculations on the OH(A, X) + Xe system, we need information about the PES correlating asymptotically with the OH(A)+Xe state, $2^2A'$, the two PESs correlating with the ground OH(X)+Xe state, $1^2A'$ and $1^2A''$, and the non-adiabatic coupling between the two adiabatic surfaces of the same $A'$ symmetry. To calculate these PESs, we have applied a multi-reference approach by selecting reference wavefunctions in state-averaged multi-configuration self-consistent field calculations (SA-MCSCF),[23] followed by the internally contracted multi-reference configuration interaction method[24] with single and double excitations, and the Davidson correction[25] that accounts for higher excitations and lowers the effects of size-inconsistency in the MRCI method (MRCISD+Q). The interaction energies are calculated without the basis set superposition error correction and are defined by subtracting the asymptotic total energy from total energies at given geometry. In addition to the non-adiabatic coupling, we have also calculated transition matrix elements of the Cartesian components of the electronic orbital angular momentum operator, $\hat{L}$, between the

OH(A)+Xe and OH(X)+Xe adiabatic electronic states (see Section II D). All electronic structure calculations are performed with the MOLPRO suite of programs.[26]

### A. Geometries, basis sets and quasi-diabatization

We describe the geometry of the Xe–O-H complex using Jacobi coordinates. The intermolecular vector, $\boldsymbol{R}$, joins the center of mass of the OH molecule and the Xe atom. The Jacobi angle, $\theta$, is defined as the angle between $\boldsymbol{R}$ and the OH diatomic vector, $\boldsymbol{r}$, with $\theta = 0°$ for the Xe–H-O collinear geometry. For all calculations, the OH monomer is kept rigid at the equilibrium geometry of the A $^2\Sigma^+$ state, $r_e = 1.012$ Å.[27] Calculations were performed for 76 intermolecular $R$ distances in the range between 2.3 $a_0$ and 50 $a_0$ and the angular grid for the $\theta$ variable consisted of 19 values (every 10°). Additional angular grid points at $\theta = 0.5, 5, 125, 145, 165, 175, 179°$ were invoked to sample the anisotropy near the $1A' - 2A'$ state crossing in more detail.

The OH molecule is placed along the $z$-axis of the Cartesian coordinate system and the Xe atom rotates on the $xz$-plane, with the $y$-axis perpendicular to the triatomic plane. The singly occupied $\pi_x$ and $\sigma_z$ orbitals of OH in the A state, which are symmetric with respect to the reflection operation in the $xz$ plane, belong to the $A'$ representation of the $C_s$ symmetry group.

In all *ab initio* calculations, we used the augmented, correlation-consistent quadruple-zeta basis set with a 28-electron-core *pseudo*-potential (denoted aug-cc-pvqz-PP) of Peterson *et al.* for the Xe atom[28] and the augmented, correlation-consistent aug-cc-pvqz basis set of Dunning for the O and H atoms.[29]

The $\pi_x$ orbital is one of the components of the doubly-degenerate ground OH(X) state and $\sigma_z$ defines the excited OH(A) state. These two electronic configurations, in the presence of the Xe atom, will belong to the same symmetry representation, $A'$, and will be coupled non-adiabatically. We have used a quasi-diabatization method,[30] as implemented in the MOLPRO program,[26] to calculate mixing angle and the diabatic off-diagonal coupling term, $H_{xz}$, and two diagonal diabats, $H_{xx}$ and $H_{zz}$. We use the method of the largest overlap with the reference orbitals that are taken at the collinear geometry for $\theta = 180°$, where the adiabatic and diabatic states coincide and are allowed to cross. The $1^2A''$ adiabatic PES coincides with the $H_{yy}$ diabat since it is the only one of such symmetry among the electronic

states considered here.

### B. Fitting of the PESs

We fitted the diabatic and adiabatic potentials and off-diagonal coupling matrix elements to analytical representations for use in quantum and *quasi*-classical dynamical calculations. The diagonal diabatic $H_{xx}$, $H_{yy}$, and $H_{zz}$ PESs and adiabatic $1^2A'$, $2^2A'$, and $1^2A''$ PESs have been expanded in a Legendre expansion by solving a system of linear equations to generate discrete sets of *ab initio* data using the linear least-square method:

$$V(R,\theta) = \sum_{\lambda=0}^{15} v_\lambda(R) P_{\lambda 0}(\cos\theta) . \tag{1}$$

The off-diagonal diabatic $H_{xz}$ PES is expanded in the associated Legendre $P_{\lambda 1}(\cos\theta)$ functions:

$$H_{xz}(R,\theta) = \sum_{\lambda=1}^{15} v_\lambda^{xz}(R) P_{\lambda 1}(\cos\theta) . \tag{2}$$

The $P_{\lambda 1}$ associated Legendre functions ensure that the diabatic coupling vanishes at $\theta = 0°$ and $\theta = 180°$.

The radial expansion coefficients, $v_\lambda(R)$, of each PES are then fit using the Reproducing Kernel Hilbert Space method[31] with radial kernel parameter $n = 2$ and a long-range extrapolation radial kernel characterized with $C_6/R^6$ asymptotics. The Fortran routines of the PESs developed in this work are available for download from the Supplementary Information.

### C. Features of the potential energy surfaces

In Table I, we show a comparison of the minima featured on the OH(X)+Xe and OH(A)+Xe MRCISD+Q PESs calculated in this work with those of the previously published OH(X)+Xe PES of Gilijamse *et al.*[19] and previous theoretical results of the OH(A)+Xe PES of Singh and Heaven[32] (presented at conference in Columbus, OH in 2009). The values of the minima on our OH(X)+Xe PES are qualitatively similar to those of Gilijamse *et al.*,[19] however, it should be noted that the OH diatomic distance used in their calculations corresponds to $r_e$ of the $X^2\Pi$ state, whereas the value used in this work corresponds to $r_e$ of the A $^2\Sigma^+$ state. The OH(X)+Xe minima are one to three orders of magnitude smaller than those on the excited OH(A)+Xe PES. The global minimum occurs for the Xe–O-H collinear

geometry ($\theta = 180°$) in the excited $2A'$ PES. It is around 1.52 eV deep with respect to the OH(A) + Xe asymptotic limit and is found fairly close to the O atom, at 4.15 $a_0$. The local minimum at the other collinear (Xe–H-O(A)) geometry ($\theta = 0°$) is four times shallower, with a well depth of 0.38 eV, and is located at $R_e = 5.55\,a_0$.

In Fig. 1, we show radial cuts of the MRCISD+Q adiabatic PESs of $A'$ symmetry (dashed lines) and the resulting diabatic PESs in nearly collinear configurations (solid lines). In the top panel, $\theta = 10°$, which is close to the Xe–H-O collinear geometry and, in the bottom panel, $\theta = 170°$, which is close to the opposite Xe–O-H geometry. The diabatic crossing occurs roughly in the middle of the global minimum of the OH(A)+Xe PES, whereas there is no diabatic crossing (at least at the repulsive energies shown in the plot) for the Xe–H-O geometry. This is very similar finding to our previous diabatic PESs obtained for the OH(A,X)+Kr coupling system[8]. In comparison to OH(A)+Xe, the global minimum of the OH(A)+Kr PES is approximately half as deep, and the diabatic A/X crossing is shifted to a smaller distance ($R_c \approx 3.8\ a_0$) in comparison to OH(A, X) + Xe (for which $R_c \approx 4.2\ a_0$).

Fig. 2 shows 3-D surface plots of the $H_{xx}$ and $H_{zz}$ diabatic PESs, oriented to expose more clearly the region of the diabatic crossing, which extends around 30° from the global minimum at $\theta = 180°$. The surface and contour plots of the off-diagonal diabatic coupling, $H_{xz}$, are shown in Fig. 3. In this figure, we also show the Xe atom approaching the O-end of the OH(A) radical towards the region of the A/X state crossing, where the coupling becomes much stronger for slightly bent geometries around the $\theta = 180°$ minimum. For the Xe–O-H collinear geometry, the $H_{zz}$ diabatic PES, corresponding to the upper OH(A)+Xe system, is crossed by the repulsive walls of the diabatic $H_{yy}$ and $H_{xx}$ PESs well below the Xe–O-H(A) asymptote, in the middle of the global minimum of the $H_{zz}$ diabat (see the bottom panel of Fig. 1). The presence of the very deep well in the Xe–O-H collinear arrangement makes the crossing energetically accessible. The other crossing for the Xe–H-O collinear geometry lies much higher in energy, well outside current experimental access. We refer the reader to the work of Lehman *et al.*[8] for details on the diabatization method used here on the OH(A,X)+Xe electronically coupled system.

### D. Coupling of the potential energy surfaces

At present, only two of the system-specific electrostatic and roto-electronic coupling matrix elements have been calculated for the OH+Xe system: $\langle 2A'|L_x|1A''\rangle$ and $\langle 2A'|L_z|1A''\rangle$. A comparison of the calculated elements for the OH+Kr and OH+Xe systems suggests that the as yet uncalculated elements for OH+Xe might be estimated by applying a shift in $R$, the Rg–OH separation, relative to those already obtained for OH+Kr. As such, the peak in intensity of the shifted coupling matrix elements with respect to $R$ then coincides well with that of the conical intersection between the OH+Xe PESs. Fig. 4 presents cross-sectional plots of the $2A'$ and $1A'$ PESs, and a selection of the matrix elements that couple them, for the OH+Xe system. In the figure, the elements in bold are the result of taking the faintly-colored elements for OH+Kr and shifting them in $R$. Fig. 5 shows all the calculated and estimated coupling matrix elements used in the theoretical calculations for the OH+Xe system presented here.

Ideally, it would have been preferable to use all the relevant matrix elements explicitly calculated for the Xe-OH system. However, it proved impossible to calculate the matrix elements of the product of electronic angular momentum operators in conjunction with the 28-electron core pseudo-potential (aug-cc-pvqz-PP). All those matrix elements involving $L^2$ were incorrectly returned as zero. Nevertheless, as will be shown in Section IV A, the results obtained including the $L^2$ matrix elements were essentially the same as those obtained neglecting them.

## III. OH(A) + Xe COLLISION DYNAMICS: METHODS

### A. Theoretical methods

As in our previous work,[3–5,7,10,18,33–35] the notation used here is as follows. In all cases, vectors are represented by bold italic symbols ($\boldsymbol{j}$), and the corresponding quantum numbers by italics ($j$).

The nuclear rotational angular momentum of OH is labeled $\mathcal{R}(\mathcal{R}')$, where primes denote quantities after a collision, and is equivalent to $\boldsymbol{N}(\boldsymbol{N'})$, the OH rotational angular momentum excluding nuclear and electron spin. This is the case because OH(A), being a $^2\Sigma^+$ state, has zero electronic orbital angular momentum and, for this reason, $\boldsymbol{N}$ is perpendicular to

This manuscript was accepted by J. Chem. Phys. Click here to see the version of record.

ing OH bond vector, $\boldsymbol{r}$. Under the Hund's case (b) coupling scheme, the nuclear spin of OH, $\boldsymbol{S}$, couples to $\boldsymbol{N}(\boldsymbol{N'})$ to form $\boldsymbol{j}(\boldsymbol{j'})$, the total angular momentum of OH (excluding nuclear spin), where $\boldsymbol{j} = \boldsymbol{N} + \boldsymbol{S}$. Since OH(A) is a doublet state ($S = 0.5$), $j = N \pm 0.5$, giving rise to two *spin-rotation* levels that are labeled $f_1$ ($j = N + 0.5$) and $f_2$ ($j = N - 0.5$). Finally, including the orbital angular momentum of the triatomic system, $\boldsymbol{\ell}(\boldsymbol{\ell'})$, gives the total angular momentum of the system, $\boldsymbol{J}$.

### B. The TSH-QCT method

Non-adiabatic trajectory surface hopping[36] *quasi*-classical trajectory (TSH-QCT) calculations were run on the OH(X,A)+Xe potentials using the fewest switches surface hopping method of Tully.[37] Two kinds of calculations were performed: a two-state model, in which trajectories are propagated over the $1^2A'$ and $2^2A'$ potentials (ignoring $1^2A''$), as used in our recent work on OH + Kr;[8,18] and a full three-state model, including all the potential energy surfaces involved in this system ($1^2A'$, $1^2A''$ and $2^2A'$) and the electronic and roto-electronic couplings between them.[11] Full details of the two methods used are presented in Refs. 8 and 18 and Ref. 11, respectively, and so only a brief summary will be given here.

Approximately $10^4 - 10^5$ trajectories were run for each initial rotational state, $N$. The O–H bond length was held constant (rigid rotor behavior) throughout the integration by the method of Lagrangian multipliers, as the potentials used here were calculated at a fixed $r_{\mathrm{OH}}$. At the end of each trajectory, the final vector angular momentum of OH, $\boldsymbol{N'}$, was converted to a quantum number, $N'$, *via* $|\boldsymbol{N'}| = \hbar\sqrt{N'(N'+1)}$, and $N'$ was binned to the nearest integer (using histogram binning). Trajectories for which $N'$ was in the range $N \pm 0.5$ were considered elastic.[18]

A further correction for the assignment of final rotational states results from the consideration of the different bond lengths in OH(X) and OH(A), with values of 0.970 Å and 1.012 Å,[27] respectively. The OH(X) products of electronic quenching are assigned a final quantum state, $N''$, by equating the rotational energies in the two electronic states,

$$N''_X = -\frac{1}{2} + \sqrt{\frac{1}{4} + \frac{N''^2_A}{x_r} + \frac{N''_A}{x_r}}\,, \tag{3}$$

with $x_r = B_X/B_A = (r_A/r_X)^2$, the ratio of the rotational constants in the two electronic states, which takes a value around 1.08.[27] The corrected $N''_X$ is binned to a quantum number,

This manuscript was accepted by J. Chem. Phys. Click here to see the version of record.

$N''$, as above.

In 'fixed-energy' calculations, the collision energy was 0.039 eV, which corresponds to the mean thermal energy at 300 K and to the calculations performed in our previous work on OH(A) + Kr.[8,18,35] The maximum impact parameter, $b_{\max}$, was set to 6.5 Å, such that all inelastic (and elastic depolarizing) collisions were included, and the impact parameter, $b$, for each trajectory was sampled according to $b_i = (\xi)^{1/2}\, b_{\max}$, where $\xi$ is a random number in the (0,1) range. Electronic quenching cross-sections were calculated in the usual way,[8,18,35]

$$\sigma_Q = \pi b_{\max}^2 \frac{\mathcal{N}_Q}{\mathcal{N}_{\rm tot}}\,, \tag{4}$$

where $\mathcal{N}_Q$ is the number of trajectories out of the total, $\mathcal{N}_{\rm tot}$, that undergo quenching.

Also presented in this paper are cross-sections for *total removal* from a given spin-rotation level $(N, j)$ in OH(A), which are the sum of the cross-sections for electronic quenching, $\sigma_Q$, and rotational energy transfer, $\sigma_j = \sum_{j' \neq j} \sigma_{jj'}$. For this purpose, *quasi*-open-shell $\sigma_j$ are calculated using the tensor opacity formalism described in detail previously.[3,6,7]

'Continuous-energy' calculations were also run, in which the collision energy for each trajectory was randomly and uniformly sampled from the range 0.001–0.125 eV, as described in Refs. 35, 38–40. For these continuous-energy calculations, $b_{\max}$ will vary with the collision energy, $E_t$. Since electronic quenching is a barrierless process, a Langevin capture-type model[41] is chosen for the behavior of $b_{\max}(E_t)$: the quenching cross-section should vary as $E_t^{-0.5}$ and, also, $\sigma_Q \sim [b_{\max}(E_t)]^2$, implying that $b_{\max}(E_t) \sim E_t^{-0.25}$. By running relatively small batches of trajectories at a series of fixed collision energies, the function $b_{\max}(E_t)$ was fitted to the form

$$b_{\max}(E_t) = A + B \times E_t^{-z}\,, \tag{5}$$

where $A = 5.8$ Å; $B = 2.8$ Å·(eV)$^z$, and $z = 0.2$. $b_{\max}$ is in Å and $E_t$ is in eV. The weight of each trajectory is given by[38–40]

$$w_i = \frac{b_{\max}^2(E_t)}{D^2}\,, \tag{6}$$

where $D$ is taken as the value of $b_{\max}(1\,\text{meV})$. Note that the value of $D$ is not important as it will cancel out in Eq. (7).

The thermal (Maxwell-Boltzmann average) quenching rate constant can be written directly as[33]

$$k_Q(T) = \frac{\pi D^2 (E_2 - E_1)}{\mathcal{N}_{\rm tot}} \sum_{i=1}^{\mathcal{N}_Q} w_i \mathcal{P}_{\rm MB}(E_t^{(i)}|T) v_{\rm rel}^{(i)}\,, \tag{7}$$

This manuscript was accepted by J. Chem. Phys. Click here to see the version of record.

where $\mathcal{P}_{\rm MB}(E_t|T)$ is the Maxwell-Boltzmann distribution of energies at temperature $T$, and $v_{\rm rel}^{(i)}$ is the relative velocity of the $i$-th trajectory. This rate constant can be turned into a thermal (flux-averaged) cross-section for electronic quenching, $\sigma_Q$, by simply dividing by the relative velocity, $\langle v_{\rm rel}(T)\rangle$. This is the quantity that is compared to experiment, as opposed to $\sigma_Q(T) \equiv \langle \sigma_Q \rangle$ (see Section III C).

The symmetry labels $1A'$ and $1A''$ for the potentials refer to reflection symmetry in the three-atom plane, defined by the $\boldsymbol{R}$ and $\boldsymbol{r}$ Jacobi vectors, and, as such, are not the same as the $\Lambda$-doublet levels, $\Pi_{A'}$ and $\Pi_{A''}$, which refer to reflection symmetry in the plane of rotation of OH (in the high-$j$ limit).[42] Therefore, trajectories ending on the $1A'$ PES after quenching do not necessarily populate $\Pi_{A'}$. Similarly, transitions from $2A' \rightarrow 1A''$ may not appear in the $\Pi_{A''}$ $\Lambda$-doublet of the OH($X^2\Pi$).

In recent papers by Perkins *et al.*[11] and Jambrina *et al.*,[43,44] a conceptually simple method has been proposed to extract the population of the $\Lambda$-doublet states from the cross-section on the $1^2A'$ and $1^2A''$ PESs. Only a brief account will be shown here; the interested reader is referred to Ref. 43 for details.

Flux conservation implies that the sum of the cross-sections on the two $\Lambda$-doublet states should be equal to the sum of the their values on each of the two competing PESs:

$$\sigma[\Pi_{A'}] = W_{A'}\,\sigma(A') + (1 - W_{A''})\,\sigma(A'')\,, \tag{8}$$

$$\sigma[\Pi_{A''}] = (1 - W_{A'})\,\sigma(A') + W_{A''}\,\sigma(A'')\,. \tag{9}$$

$\sigma(A')$ and $\sigma(A'')$ refer to the cross-section calculated on the $A'$ PES or $A''$ PES, respectively, and $\sigma[\Pi_{A'}]$ and $\sigma[\Pi_{A''}]$ are the respective cross-sections populating the two $\Lambda$-doublet levels. The weighting coefficients in Eq. (8), $W_{A'}$ and $W_{A''}$, connect the results on a given PES and the assignment to one of the $\Lambda$-doublet product states. As shown in Ref. 43, these coefficients are related to the dihedral angle, $\theta_{\boldsymbol{uj'}}$, between the OH($^2\Pi$) molecular rotational plane and the plane defined by the three atoms. $\boldsymbol{j'}$ denotes the product rotational angular momentum, which classically is perpendicular to the diatom plane of rotation, and $\boldsymbol{u}$ stands for the vector normal to the three-atom plane defined by diatom internuclear vector, $\boldsymbol{r}$, and the relative recoil velocity, $\boldsymbol{k'}$.[11]

The weights $W_{A'}$ and $W_{A''}$ can be obtained by averaging $\cos^2\theta_{\boldsymbol{j'u}}$ over one rotational period for calculations on the $A'$ and $A''$ PESs, and over the ensemble of trajectories leading

ing a specific final state:

$$W_{A'} = \langle\langle \cos^2 \theta_{\boldsymbol{j'u}} \rangle_{\rm rot} \rangle_{A'}, \tag{10}$$

$$W_{A''} = \langle\langle \cos^2 \theta_{\boldsymbol{j'u}} \rangle_{\rm rot} \rangle_{A''}. \tag{11}$$

It has been shown that the average value of the square cosine of $\theta_{\boldsymbol{j'u}}$, $\langle \cos^2 \theta_{\boldsymbol{j'u}} \rangle_{\rm rot}$, is related to the projection of $\boldsymbol{j'}$ on the products recoil direction, $\boldsymbol{k'}$, through the expression:[43]

$$\langle \cos^2 \theta_{\boldsymbol{j'u}} \rangle_{\rm rot} = 1 - \left| \cos^2 \theta_{\boldsymbol{k'j'}} \right|^{1/2}, \tag{12}$$

such that

$$W_{A'} = 1 - \langle \cos^2 \theta_{\boldsymbol{k'j'}} \rangle^{1/2} \approx 1 - \left[ \frac{2}{3} a_0^{(2)} + \frac{1}{3} \right]^{1/2}, \tag{13}$$

in which $a_0^{(2)}$, the alignment moment of $\boldsymbol{j'}$ with respect to $\boldsymbol{k'}$, which is the average value of the second degree Legendre polynomial, $\langle P_2(\cos \theta_{\boldsymbol{k'j'}}) \rangle$, has been calculated on the $A'$ PES. An identical expression holds for $W_{A''}$ when $a_0^{(2)}$ is calculated on the $A''$ PES.

The advantage of Eq. (13) is that $\cos^2 \theta_{\boldsymbol{k'j'}}$ can be calculated asymptotically without needing to average over rotational periods. The weights are then determined by averaging over the ensemble of trajectories that lead to a given final state. In addition, Eq. (13) shows that the $\boldsymbol{k'}$-$\boldsymbol{j'}$ correlation relates the Λ-doublet populations to reactivity on the $A'$ and $A''$ PESs.

Negative values of $a_0^{(2)}$, close to its lower limit, $-1/2$, correspond to $\boldsymbol{j'} \perp \boldsymbol{k'}$ and $|\cos \theta_{\boldsymbol{k'j'}}| \approx 0$, while positive values, close to one, imply that $\boldsymbol{j'} || \boldsymbol{k'}$. According to Eq. (13), $a_0^{(2)} \approx +1$ are associated with weight factors close to zero; that is, products on the $A'$ PES would appear as the $\Pi(A'')$ Λ-doublet state and *vice versa*. When $a_0^{(2)} \approx -1/2$, the weight factor tends to 1, and products on the $A'$ PES would correspond to the $\Pi(A')$ Λ-doublet state (and equivalently for the $A''$ PES). Since the reaction stereodynamics is closely linked to the collision mechanism, it is then possible to trace the relative population of Λ-doublet states to reaction mechanisms and possibly to specific features of the PESs involved.

### C. Experimental methods

As in our previous work,[3–5,10,18,34,35] Zeeman quantum beat spectroscopy, a form of polarized laser-induced fluorescence, was used to measure rates for electronic quenching and

This manuscript was accepted by J. Chem. Phys. Click here to see the version of record.

total removal from a given $(N, j)$ level of OH(A) at a temperature of 300 K. Only the loss of population is dealt with in this paper; polarization is left for a future paper.[45]

Ground state OH radicals were produced from the photolysis of nitric acid by 193 nm, pulsed, unpolarized excimer laser radiation.[46,47] Helium carrier gas was bubbled through a 2:3 mix of 98% sulfuric acid and 70% nitric acid, with the sulfuric acid serving to reduce the vapor pressure of water.[1,48] From similar procedures in the literature, $HNO_3$ is believed to make up 3-5% of the flow.[1,46,48–50]

The helium/acid mix was flowed through a stainless steel vacuum chamber at a mass flow rate of 2 to 3 sccm (standard $cm^3$ per minute), with a separate flow of Xe collider, adjustable from 3 to 10 sccm. These flows were kept as low as possible to avoid using too much expensive Xe gas, but high enough to ensure a fresh volume was probed on each laser shot. After a delay of 10–30 $\mu$s to allow the nascent OH(X) radicals to translationally thermalize through collisions, they were excited to specific $(N, j)$ levels of the $A^2\Sigma^+$ state by counter-propagating pulsed, tunable Nd:YAG-pumped dye-laser radiation on the (0,0) band of the OH(A←X) transition (around 306 nm). The linear polarization of this laser radiation was improved using a Glan-Taylor prism, and switched between polarization that was parallel and perpendicular to the fluorescence detection direction on alternate shots using a photoelastic modulator. The purity of this polarisation was found to be better than 95% on exit of the chamber. All of the experiments described here were performed without a magnetic field present. The center of the vacuum chamber was shielded with $\mu$-metal to null the Earth's magnetic field, as well as other stray fields, and checked with a Hall probe.

The spontaneous fluorescence from OH(A) was focused onto the entrance slits of a monochromator, preceded by a Glan-Taylor linear polariser. Low resolution could be selected to measure fluorescence from all final rotational levels of OH(A) and so obtain electronic quenching cross-sections, or emission from a single spin-rotation state could be measured to obtain total removal cross-sections. The resolved fluorescence was collected by a photomultiplier tube and the resulting signal was sent to an oscilloscope and PC. As in our previous studies, the response time of the system described here was tested and found to be less than 20 ns.[35]

This manuscript was accepted by J. Chem. Phys. Click here to see the version of record.

### D. Data analysis

As described in the previous section, fluorescence traces were recorded with the probe-laser polarisation parallel to the detection direction ($I_\parallel$) and perpendicular to it ($I_\perp$). As no magnetic field was used in these experiments, the sum $I_\parallel + 2I_\perp$ contains no polarization contribution and is sensitive to the decay in population only.[35] The summed fluorescence signal, $I(t)$, is fitted to a single exponential for the first 100 ns, this short time being chosen to avoid the effects of secondary collisions, as shown in Fig. 6:

$$I(t) = A\,\mathrm{e}^{-(k_0+k_1[\mathrm{Xe}])\,t}\,. \tag{14}$$

In this equation, $k_0$ is the inverse of the fluorescence lifetime and $k_1$ is the rate constant either for electronic quenching, $k_Q$ (in the case when the fluorescence is not resolved), or total removal, $k_Q + k_j$ (when emission from a single $(N, j)$ state is resolved). These rate constants are converted into absolute, thermally averaged (300 K) cross-sections by dividing by the mean thermal relative velocity:

$$\sigma_Q = \frac{k_Q}{\langle v_{\mathrm{rel}} \rangle}\,. \tag{15}$$

Errors are given as one standard deviation of repeated results to allow for comparison with literature data.[1]

## IV. OH(A) + Xe COLLISION DYNAMICS: RESULTS AND DISCUSSION

### A. Electronic quenching

Experimental cross-sections for electronic quenching of OH(A) by Xe are presented in Fig. 7 and Table II and are compared to data for OH(A) + Kr[8,35] and to literature data.[1] The agreement with the data of Hemming *et al.* is seen to be excellent, and there is no observable difference between the quenching cross-sections for the $f_1$ and $f_2$ spin-rotation manifolds.

A fall in the magnitude of the quenching cross-sections with increasing rotation is observed for both OH(A) + Kr and OH(A) + Xe. As $N$ increases, collisions en route to the deep linear Rg–OH well – low on the repulsive wall in the case of OH(A) + Kr,[8,11] and near the bottom of the well for OH(A) + Xe – where the crossing takes place, are deviated, especially

at high impact parameters that become less effective with increasing rotation. Because the strongly coupled region is more accessible for OH(A) + Xe than for OH(A) + Kr, the quenching cross-sections are larger and also extend to higher $N$, remaining non-zero out to the highest rotational states measured. It is important to note that the reduced masses of the OH(A) + Kr and OH(A) + Xe systems are too similar for kinematic effects to play much of a part in the differences between these two systems.

Fig. 8 compares the experimental OH(A) + Xe quenching cross-sections with theoretical values calculated using the potentials and couplings presented in this paper. The two panels show calculations that were run at a fixed collision energy (left) or using a Maxwell-Boltzmann distribution of energies at 300 K (right). In the left panel, a comparison is also made between the results of fixed-energy calculations that were run using the two-state and three-state models discussed in Section III B. Notably, the three-state data shown in the panel on the left were generated from a model that included only the $\langle 2A'|L_x|1A''\rangle$ and $\langle 2A'|L_z|1A''\rangle$ roto-electronic coupling matrix elements that were calculated specifically for the OH+Xe system. The three-state calculation results shown in the panel on the right were generated from a model that included these calculated roto-electronic coupling matrix elements as well as the remaining elements that were estimated from those of OH+Kr.

A consideration of the fixed-energy data reveals that the three-state model (which includes the $1A''$ electronic state for the first time) results in more quenching than that predicted by the two-state model. However, both models severely underestimate the magnitude of experimental quenching. In contrast to what is observed in the case of OH(A) + Kr,[8,11] using a continuous distribution of collision energies (rather than a single, fixed collision energy) results in noticeably increased electronic quenching and improved agreement with experiment for OH(A) + Xe, especially for low rotational quantum numbers. It is important to determine the extent to which the increase in the magnitude of the calculated quenching cross-sections seen between the left- and right-hand panels of Fig. 8 is due to the use of a distribution of collision energies or the inclusion of a greater number of coupling matrix elements in the TSH calculations. To that end, Fig. 9 presents a comparison of quenching cross-sections for the OH(A)+Xe system that were generated from calculations run using: a fixed-collision-energy, three-state model that included only the calculated $\langle 2A'|L_x|1A''\rangle$ and $\langle 2A'|L_z|1A''\rangle$ roto-electronic coupling matrix elements; a variable-collision-energy, three-state model that included only the calculated $\langle 2A'|L_x|1A''\rangle$ and $\langle 2A'|L_z|1A''\rangle$ roto-electronic

This manuscript was accepted by J. Chem. Phys. Click here to see the version of record.

coupling matrix elements; and a variable-collision-energy, three-state model that included both the calculated roto-electronic coupling matrix elements and the remaining elements that were estimated from those of OH+Kr. The data reveal that, for $N = 2$ and $N = 8$, the increase in the magnitude of the quenching cross-section can be attributed almost entirely to the use of the variable-collision-energy (rather than the fixed-collision-energy) algorithm. For these states, the quenching cross-section remains virtually constant upon the subsequent addition of the remaining coupling matrix elements. For the $N = 4$ and $N = 6$ states, both the use of the variable-collision-energy algorithm and the inclusion of additional matrix elements lead to an increase in the magnitude of the quenching cross-section, however, the former factor is seen to be the more significant.

Fig. 10 shows the dependence of $\sigma_Q$ (from calculations run using the most complete three-state model) on collision energy and reveals that quenching is most prevalent in low-energy collisions that mainly sample the more attractive part of the potential energy surface, where coupling is stronger. On the other hand, high-energy collisions, which preferentially sample the repulsive potential wall, tend to result in less quenching. In addition, low-energy trajectories are more likely to be trapped in the deep well of the $2A'$ PES in the Xe–O-H geometry than those with higher energy collision energy. In any case, the data further emphasize the importance of carrying out a proper averaging of $\sigma_Q$ over the collision energy if the full extent of the electronic quenching that is observed experimentally is to be accounted for by theoretical calculations.

Even for the most complete, three-state, variable-collision-energy theoretical model, the calculated quenching cross-sections still underestimate the experimental data, and fall off too quickly with increasing $N$. Reasons for the discrepancy between theory and experiment are more likely to lie on the theoretical side, given the good agreement between the present experimental results and data previously recorded elsewhere.[1] Spin-orbit coupling is not included in the semiclassical theory used here, and it would be interesting to see how much difference this would make to the results – it is predicted to be a somewhat more important effect for OH(A) + Xe than for OH(A) + Kr. The molecular OH(X) spin-orbit splitting in Xe-OH will be $(R, \theta)$-dependent and may vary significantly close to the A-X crossing at the $\theta = 180°$ geometry. This coupling might be an additional source of electronic quenching flux, but in our semi-classical dynamical model it has been neglected. A further source of the disagreement is the approximate nature of the electronic structure and dynamical calcu-

lations performed here – the potentials and electrostatic couplings were obtained assuming that the $1A''$ surface was uncoupled to the two PESs of $A'$ symmetry (the $A''$ and $A'$ surfaces would be coupled by the spin-orbit interaction), with roto-electronic couplings incorporated into the theory afterwards.

Fig. 11 shows the experimental cross-sections for *total removal* (the sum of electronic quenching and rotational energy transfer) as a function of the initial rotational number, $N$, for the $f_1$ and $f_2$ states (left and right panels, respectively). These results are compared with QM and QCT adiabatic calculations for rotational energy transfer on the upper $2A'$ PES, and with total removal data obtained from the three-state TSH model. Interestingly, but probably not unexpectedly, QM and QCT adiabatic calculations for rotational energy transfer (RET) on the upper $2A'$ PES account fairly well for the experimental total removal in spite of the fact that no quenching can take place in these particular theoretical models. This seems to indicate that, in single-surface calculations, trajectories that visit the well on the $2A'$ surface and that would otherwise experience crossing to $1A'$ or $1A''$ instead give rise to RET. In turn, the sum of the quenching and RET cross-sections predicted by the three-state TSH model also agrees fairly well with the experimental total removal data and with the adiabatic RET calculations – even though, as shown earlier, quenching cross-sections are underestimated in the TSH model. Therefore, it seems that the TSH method predicts the correct number of trajectories that enter the Xe–OH well; however, the ratio of how many trajectories end up on the $1A'$ and $1A''$ PESs after quenching to how many remain on the $2A'$ PES (eventually giving rise to OH(A)+Xe inelastic scattering) is incorrect. This may suggest an error in the couplings, rather than in the potentials themselves, or a failure of the TSH-QCT model to fully account for quenching.

It is important to bear in mind that some of the coupling matrix elements used in the most complete model discussed here were estimated from those of OH+Kr, although the results obtained with only the $L_x$ and $L_z$ matrix elements (which were calculated specifically for OH+Xe) do not differ much from those including estimates of the remaining couplings elements. Therefore, it would be desirable to calculate and implement a full set of roto-electronic coupling matrix elements, and geometry-dependent spin-orbit coupling matrix elements, for OH+Xe into the variable-collision-energy, three-state TSH QCT algorithms.

### B. OH(X) product state distributions

As well as the cross-sections for electronic quenching, it is also possible to study the product state distributions from non-adiabatic collisions. To that end, the rotational and Λ-doublet state distributions of the OH(X) products of quenching provide a wealth of information about the conical intersection region and passage through it.[8,9]

As already described in Section III B, Jambrina *et al.* have presented a methodology by which the reaction products on a given PES of symmetry $A'$ or $A''$ can be related to the respective Λ-doublet states of the open-shell diatomic product that are populated after the collision.[43] Specifically, a trajectory terminating on one of the two PESs can be assigned with different weights to each of the two Λ-doublet states.[44] In the present case, it is found that the rotational momentum vector of OH(X) after the collision is strongly polarized perpendicularly to the recoil velocity (cartwheel motion). Therefore, the polarization parameter $a_0^{(2)}$ is close to $-1/2$ for trajectories terminating on the two PESs. As it happens, for the OH(A)+Xe system, the rotational plane of the OH radical coincides with the OH–Xe triatomic plane to a large extent. Hence, the respective weights, $W_{A'}$ and $W_{A''}$, are close to one, which implies that, for the most part, $A' \rightarrow \Pi_{A'}$ and $A'' \rightarrow \Pi_{A''}$. This is well illustrated in Fig. 12 which shows that the rotational distributions calculated for trajectories ending on the $A'$ and $A''$ are fairly similar to those obtained by assigning those same trajectories to the Λ-doublet states, and that the weight factors are nearly independent of the final rotational state. This result is hardly surprising considering that the $1A'$ and $1A''$ are degenerate at 180°, which is where the crossing takes place. A sudden release of energy occurs after quenching, and a torque is consequently imparted to the outgoing OH fragment for which the plane of rotation remains the same as the three-atom plane. Such behavior is similar to that found in the quenching of OH+Kr,[11] but is in stark contrast to that experimentally observed and calculated for the O($^3P$)+$D_2$ reaction,[43] or that calculated for the O($^3$P)+$N_2$ or the O($^3$P)+HCl reactions,[44] which exhibit a very significant 'transfer' of population from the A″ PES to the $\Pi_{A'}$ Λ-doublet.

Although not measured experimentally in the work reported here, it is helpful to determine a quantitative measure of preferential Λ-doublet population, as predicted by TSH QCT calculations, by determining the *degree of electron alignment* (DEA). This is defined

$$\mathrm{DEA} = \frac{\sigma_{N''}(\Pi_{\mathrm{A}'}) - \sigma_{N''}(\Pi_{\mathrm{A}''})}{\sigma_{N''}(\Pi_{\mathrm{A}'}) + \sigma_{N''}(\Pi_{\mathrm{A}''})}. \tag{16}$$

Positive values of the DEA (that range between 0 and +1) imply a preference for population of the $\Pi_{A'}$ $\Lambda$-doublet (and, in this case, also for the 1A′ PES); negative values (that range between 0 and −1) imply a preference for population of the $\Pi_{A''}$ $\Lambda$-doublet.

Fig. 13 shows the OH(X) product rotational-state distributions of OH(A)+Xe trajectories whose initial state on the $2A''$ excited PES are the indicated OH(A, $N$) rotational levels. The top and middle panels represent the cross-sections for specific OH(X, $N''$) rotational levels of the ground electronic state in the $\Pi_{A'}$ and $\Pi_{A''}$ $\Lambda$-doublet states, respectively. These calculations were run using the most complete, variable-collision-energy, three-state TSH model. The bottom panel shows the DEA calculated from Eq. (16) for the indicated OH(X, $N''$) ← OH(A, $N$) transitions.

As is the case for quenching collisions of OH+Kr,[8] for OH+Xe the OH(X) quantum state population distributions for the two $\Lambda$-doublet manifolds are rotationally hot, reflecting the strong torques experienced by the OH molecules on passage through the conical intersection. It can also be expected that the vast majority of collisions terminate in OH(X, $v'' = 0$), as is the case for the measured vibrational distribution for OH+Kr. In general, notice that the rotational-state distribution in the $\Pi_{A''}$ $\Lambda$-doublet is markedly broader than that in $\Pi_{A'}$ (see Fig. 13). This is due to the fact that the $\Pi_{A''}$ $\Lambda$-doublet is mainly populated by trajectories on the $1A''$ PES resulting from roto-electronic coupling mechanisms. In contrast, the $\Pi_{A'}$ $\Lambda$-doublet is mainly populated by trajectories ending on the $1A'$ PES, which is connected to the $2A'$ PES by electrostatic and roto-electronic couplings. The result is a sharp peak at intermediate $N''$ and a predominance for populating $\Pi_{A'}$ in the 20–30 $N''$ interval, irrespective of the initial rotational state, $N$, on the $2A'$ PES, as can be seen in lower panel of Fig. 13. The integral cross-section falls as $N$ increases, reflecting the trend shown by the non-adiabatic quenching data discussed earlier. Note that as $N$ increases, the mean value of the ground-state rotational quantum number also becomes larger, a trend which is seen for both the $\Pi_{A'}$ and $\Pi_{A''}$ $\Lambda$-doublets.

## V. CONCLUSIONS

New, multi-reference *ab initio* potential energy surfaces for the interaction of OH(X) and OH(A) with Xe have been presented, together with the couplings between them. The OH(A)+Xe $2A'$ PES, like the corresponding OH(A)+Kr potential reported previously,[35] has very deep attractive wells in both linear configurations, with the Xe–OH interaction being as strong as a chemical bond. However, the potential displays extensive angular anisotropy, with strong repulsion in side-on geometries. The OH(A) + Xe PES also has a longer range than the OH(A)+Kr PES of Ref. 35.

The ground state OH(X) + Xe potentials, $1A'$ and $1A''$, agree closely with those of Ref. 19, and are much less attractive than the excited state PES. The strongest attraction on the $1A'$ and $1A''$ PESs is of the order of hundreds of wavenumbers (rather than 12300 $cm^{-1}$ for Xe–OH(A)) and appears in the Xe–HO geometry, with an additional shallower well in T-shaped configuration on the $1A'$ PES.

At geometries corresponding to attractive Xe–OH(A) well on the the $2A'$ PES, the Xe–OH(X) potential is strongly repulsive. In the linear configuration, the ground $2A'$ and excited $1A'$ potentials have a conical intersection, with the crossing being avoided away from linearity. This intersection is located close to the bottom of the Xe—OH(A) well, making it more accessible than the analogous feature of the OH(A)+Kr PES. On passing through the conical intersection, the complex falls down the steeply repulsive part of the OH(X)+Xe potential, resulting in translationally and rotationally hot radicals. There is also a strong correlation between the ground-state PESs, $1A'$ or $1A''$, on which a given trajectory finishes after the crossing and the Λ-doublet state, $\Pi_{A'}$ or $\Pi_{A''}$, which are populated.

Cross-sections for electronic quenching and total removal from a given $(N, j)$ state have been measured experimentally for OH(A) + Xe and compared to surface hopping QCT calculations that include all three $2A'$, $1A'$ and $1A''$ potentials with electronic and roto-electronic couplings. Good agreement is seen between theoretical and experimental *total* removal cross-sections, but theory underestimates the true extent of quenching, particularly at low $N$. It is, therefore, recommended that future studies will pay special attention to the couplings between the potentials reported here. It would also be of interest to calculate the geometry-dependent spin-orbit coupling matrix elements. These matrix elements have been neglected thus far in our semi-classical dynamic model and might provide an additional source of

quenching flux. This is a topic that would deserve future investigation. A further origin of the observed discrepancies may lie on the fact that calculations have been carried out assuming that OH can be described a rigid rotor; although this assumption is adequate for adiabatic calculations, it might be a poor approximation in the case of hopping between different PES.

A future companion work to this paper will focus on rotational energy transfer and collisional depolarization of OH(A) + Xe, with particular emphasis on the competition between electronically adiabatic and non-adiabatic collision pathways.

## SUPPLEMENTARY MATERIAL

See the Supplementary Material for the Fortran routines of Xe-OH diabatic and adiabatic PESs and associated $\hat{L}^2$ and $\hat{L}$ transition matrix elements. The following files are provided in `Potential_energy_surface.tar` archive:

1. `xeoh_x_1Abis_mrcisdq_avqzpp_pes_fit.f`: Diabatic Xe-OH $H_{yy} = 1A''$ MRCISD+Q Potential Energy Surface fit routine.

2. `xeoh_x_a_adiabats.f`: Xe-OH $1A'$, $2A'$ adiabatic PESs and $H_{xx}$, $H_{zz}$ and $H_{12}$ PES fit routine.

3. `pes_evaluate.f`: Example routine to print out the Xe-OH PES values on a grid or $(R, \theta)$ in units of bohr and degrees with output energies in $\mathrm{cm}^{-1}$.

4. `Xe-OH-PESs.output`: Example output file from from the `pes_evaluate.f` routine.

5. `interpol.f`: Interpolation function.

6. `XeOH_X_A_Lxx_Mat_El_shift.dat`: Transition matrix elements of the $\hat{L}_x$ operator in atomic units.

7. `XeOH_X_A_Ly2_Lx2_Mat_El_shift.dat`: Transition matrix elements of $\hat{L}_y^2$ and $\hat{L}_x^2$ operators in atomic units.

8. `XeOH_X_A_Lz2_LxLz_Mat_El_shift.dat`: Transition matrix elements of $\hat{L}_z^2$ and $\hat{L}_x\hat{L}_z$ operators in atomic units.

9. `XeOH_X_A_Lxyz_Mat_El.dat`: Transition matrix elements of $\hat{L}_x$, $\hat{L}_y$ and $\hat{L}_z$ operators in atomic units.

10. `xeoh_lmatrix.f90`: Fortran 90 file for interpolating transition matrix elements for use in QCT-TSH scattering.

11. `README.txt`: File with above information and example of compilation of `pes_evaluate.f` routine.

## ACKNOWLEDGMENTS

The support of the UK EPSRC (to M.B. *via* Programme Grant Nos. EP/G00224X/1 and EP/L005913/1), and the Spanish Ministry of Economy and Innovation (grant CTQ2015-65033-P, MINECO/FEDER) are gratefully acknowledged. We also acknowledge also financial support from the US National Science Foundation through Grant No. CHE-1565872.

## REFERENCES

[1]B. L. Hemming, D. R. Crosley, J. E. Harrington, and V. Sick, J. Chem. Phys **115**, 3099 (2001).

[2]G. Paterson, M. L. Costen, and K. G. McKendrick, Int. Rev. Phys. Chem. **31**, 69 (2012).

[3]F. J. Aoiz, M. Brouard, C. J. Eyles, J. Kłos, and M. P. de Miranda, J. Chem. Phys. **130**, 044305 (2009).

[4]M. Brouard, A. Bryant, Y.-P. Chang, R. Cireasa, C. J. Eyles, A. M. Green, S. Marinakis, F. J. Aoiz, and J. Kłos, J. Chem. Phys. **130**, 044306 (2009).

[5]M. Costen, R. Livingstone, K. McKendrick, G. Paterson, M. Brouard, H. Chadwick, Y.-P. Chang, C. J. Eyles, F. Aoiz, and J. Kłos, J. Phys. Chem. A **113**, 15156 (2009).

[6]M. Brouard, H. Chadwick, C. J. Eyles, F. J. Aoiz, and J. Kłos, J. Chem. Phys. **135**, 084305 (2011).

[7]M. Brouard, H. Chadwick, Y.-P. Chang, C. J. Eyles, F. J. Aoiz, and J. Kłos, J. Chem. Phys. **135**, 084306 (2011).

[8]J. H. Lehman, M. I. Lester, J. Kłos, M. H. Alexander, P. J. Dagdigian, D. Herráez-Aguilar, F. J. Aoiz, M. Brouard, H. Chadwick, T. Perkins, and S. A. Seamons, J. Phys. Chem. A **117**, 13481 (2013).

[9]J. H. Lehman and M. I. Lester, Ann. Rev. Phys. Chem. **65**, 537 (2014).

[10]H. Chadwick, M. Brouard, T. Perkins, and F. J. Aoiz, Int. Rev. Phys. Chem. **33**, 79 (2014).

[11]T. Perkins, D. Herráez-Aguilar, G. McCrudden, J. Kłos, F. J. Aoiz, and M. Brouard, J. Chem. Phys. **142**, 144307 (2015).

[12]D. R. Bates and M. Nicolet, J. Geophys. Res. **106**, 1385 (1950).

[13]P. O. Wennberg, R. C. Cohen, N. L. Hazen, L. B. Lapson, N. T. Allen, T. F. Hanisco, J. F. Oliver, N. W. Lanham, J. N. Demusz, and J. G. Anderson, Rev. Sci. Instrum. **65**, 1858 (1994).

[14]D. R. Crosley, J. Atmos. Sci. **52**, 3299 (1995).

[15]M. J. Pilling and P. W. Seakins, *Reaction Kinetics* (OUP, 1997).

[16]G. Paterson, M. L. Costen, and K. G. McKendrick, Mol. Phys. **109**, 2565 (2011).

[17]G. O. Ildiz, C. M. Nunes, N. Kus, and R. Fausto, J. Chem. Phys. **137**, 064309 (2012).

[18]H. Chadwick, M. Brouard, Y.-P. Chang, C. J. Eyles, G. McCrudden, T. Perkins, S. A. Seamons, J. Kłos, M. H. Alexander, P. J. Dagdigian, D. Herráez-Aguilar, and F. J. Aoiz, J. Chem. Phys. **140**, 054306 (2014).

[19]J. J. Gilijamse, S. Hoekstra, S. Y. T. van de Meerakker, G. C. Groenenboom, and G. Meijer, Science **313**, 1617 (2006).

[20]G. Paterson, S. Marinakis, J. Kłos, M. L. Costen, and K. G. McKendrick, Phys. Chem. Chem. Phys. **11**, 8804 (2009).

[21]G. Paterson, S. Marinakis, M. L. Costen, and K. G. McKendrick, Phys. Chem. Chem. Phys. **11**, 8813 (2009).

[22]G. Sarma, A. K. Saha, J. J. ter Meulen, D. H. Parker, and S. Marinakis, J. Chem. Phys. **142**, 084309 (2015).

[23]P. J. Knowles and H.-J. Werner, Chem. Phys. Lett. **115**, 259 (1985).

[24]H.-J. Werner and P. J. Knowles, J. Chem. Phys. **89**, 5803 (1988).

[25]S. R. Langhoff and E. R. Davidson, Int. J. Quantum Chem. **8**, 61 (1974).

[26]MOLPRO, version 2012.1, a package of *ab initio* programs written by H.-J. Werner, P. J. Knowles, G. Knizia, F. R. Manby, M. Schütz and others, `http://www.molpro.net`.

[27]K. P. Huber and G. Herzberg, *Molecular Spectra and Molecular Structure: IV. Constants of Diatomic Molecules* (Van Nostrand Reinhold, 1979).

[28]K. A. Peterson, D. Figgen, E. Goll, H. Stoll, and M. Dolg, J. Chem. Phys. **119**, 11113 (2003).

[29]T. H. Dunning, Jr., J. Chem. Phys. **90**, 1007 (1989).

[30]D. Simah, B. Hartke, and H.-J. Werner, J. Chem. Phys. **111**, 4523 (1999).

[31]T.-S. Ho and H. Rabitz, J. Chem. Phys. **104**, 2584 (1996).

[32]V. B. Singh and M. C. Heaven, (2009), "Ab initio potential energy surface for the Xe-OH interaction", 64$^{th}$ OSU International Symposium on Molecular Spectroscopy, June 22-26, Columbus, OH.

[33]J. Kłos, M. H. Alexander, M. Brouard, C. J. Eyles, and F. J. Aoiz, J. Chem. Phys. **129**, 054301 (2008).

[34]M. Brouard, H. Chadwick, Y.-P. Chang, R. Cireasa, C. J. Eyles, A. O. L. Via, N. Screen, F. J. Aoiz, and J. Kłos, J. Chem. Phys. **131**, 104307 (2009).

[35]H. Chadwick, M. Brouard, Y.-P. Chang, C. J. Eyles, T. Perkins, S. A. Seamons, J. Kłos, M. H. Alexander, and F. J. Aoiz, J. Chem. Phys. **137**, 154305 (2012).

[36]J. C. Tully and R. K. Preston, J. Chem. Phys. **55**, 562 (1971).

[37]J. C. Tully, J. Chem. Phys. **93**, 1061 (1990).

[38]F. J. Aoiz, L. Bañares, T. Díez-Rojo, V. J. Herrero, and V. S. Rábanos, J. Phys. Chem. **100**, 4071 (1996).

[39]F. J. Aoiz, L. Bañares, V. J. Herrero, V. S. Rábanos, and L. Tanarro, J. Phys. Chem. A **101**, 6165 (1997).

[40]F. J. Aoiz, L. Bañares, and V. J. Herrero, J. Chem. Soc. Faraday Trans. **94**, 2483 (1998).

[41]P. Langevin, Ann. Chim. Phys. **5**, 245 (1905).

[42]M. H. Alexander, P. Andresen, R. Bacis, R. Bersohn, F. J. Comes, P. J. Dagdigian, R. N. Dixon, R. W. Field, G. W. Flynn, K.-H. Gericke, E. R. Grant, B. J. Howard, J. R. Huber, D. S. King, J. L. Kinsey, K. Kleinermanns, K. Kuchitsu, A. C. Luntz, A. J. McCaffery, B. Pouilly, H. Reisler, S. Rosenwaks, E. W. Rothe, M. Shapiro, J. P. Simons, R. Vasudev, J. R. Wiesenfeld, C. Wittig, and R. N. Zare, J. Chem. Phys. **89**, 1749 (1988).

[43]P. G. Jambrina, A. Zanchet, J. Aldegunde, M. Brouard, and F. J. Aoiz, Nat. Comm. **7**, 13439 (2016).

[44]B. G. Jambrina, M. M., Zanchet, G. E., and F. J. Aoiz, J. Phys. Chem. A **122**, 2739 (2018).

[45]M. Brouard, G. McCrudden, T. Perkins, S. A. Seamons, F. J. Aoiz, D. Herráez-Aguilar, and J. Kłos, (2018), in preparation.

[46]Q. Li, R. T. Carter, and J. R. Huber, Chem. Phys. Lett. **334**, 39 (2001).

[47]J. R. Huber, ChemPhysChem **5**, 1663 (2004).

[48]B. L. Hemming and D. R. Crosley, J. Phys. Chem. A **106**, 8992 (2002).

[49]T. L. Myers, N. R. Forde, B. Hu, D. C. Kitchen, and L. J. Butler, J. Chem. Phys. **107**, 5361 (1997).

[50]N. Herath, S. C. Everhart, A. G. Suits, and O. S. Vasyutinskii, J. Chem. Phys. **134**, 034311 (2011).

[51]N. J. Turro, V. Ramamurthy, and J. C. Scaiano, *Principles of molecular photochemistry: an introduction* (University Science Books, 2009).

| OH(X) + Xe | | $\theta$ / ° | $R_e$ / $a_0$ | $E_{min}$ / $cm^{-1}$ |
|---|---|---|---|---|
| MRCISD+Q | This work | 0 | 7.60 | -200.5 |
| | | 180 | 7.40 | -106.6 |
| $A'$ | | 80 | 6.70 | -180.0 |
| RCCSD(T) | Ref. 19 | 0 | 7.60 | -202.5 |
| | | 180 | 7.40 | -117.8 |
| $A'$ | | 84 | 6.44 | -224.4 |
| OH(A) + Xe | | $\theta$ / ° | $R_e$ / $a_0$ | $E_{min}$ / $cm^{-1}$ |
| MRCISD+Q | This work | 0 | 5.55 | -3028 |
| | | 180 | 4.15 | -12258 |
| MRCISD+Q | Ref. 32 | 0 | 5.20 | -2324 |
| | | 180 | 4.25 | -11900 |

TABLE I. Comparison of the minima of the OH(X) + Xe PES obtained in this work with PES of Gilijamse *et al.*[19] Global ($\theta = 180°$) and local ($\theta = 0°$) minima of the OH(A) + Xe PES obtained in this work are also compared with the values obtained by Singh and Heaven[32]. Note that the values of Singh and Heaven are calculated for the distance corresponding to the equilibrium bond length of OH(X), 0.97 Å. All energies are expressed relative to the asymptotic limit of the corresponding electronic state.

| | $\sigma_Q$ / Å$^2$ | | | |
|---|---|---|---|---|
| $N$ | $f_1$ | $f_2$ | Hemming[1] | TSH-QCT |
| 0 | 22(1) | – | – | 18 |
| 1 | 28(3) | – | – | – |
| 2 | 28(1) | 30(1) | – | 24 |
| 3 | 27(8) | 28(2) | – | 24 |
| 4 | – | 32(3) | – | 20 |
| 5 | 30(1) | 32(3) | – | 16 |
| 6 | – | 21(2) | 25(1) | 14 |
| 7 | 25(1) | – | – | 12 |
| 8 | – | 25(2) | – | 10 |
| 9 | – | 26(1) | – | 7 |
| 10 | 22(4) | 18(1) | 22(2) | 6 |
| 11 | – | – | – | 4 |
| 12 | – | – | – | 2 |
| 13 | – | – | 16(1) | – |
| 14 | – | – | – | 1 |
| 15 | – | – | 12(1) | 1 |

TABLE II. Cross-sections for electronic quenching of OH(A) by Xe under thermal conditions (300 K). The three-state TSH-QCT calculations were performed using a 300 K Maxwell-Boltzmann average over a continuous range of collision energies ($0.005 - 0.125$ eV). The error bars (indicated in brackets on the experimental data) were determined using one standard deviation of repeated results. Note that the spin-rotation level employed by Hemming *et al.* was not specified in their paper.[1]

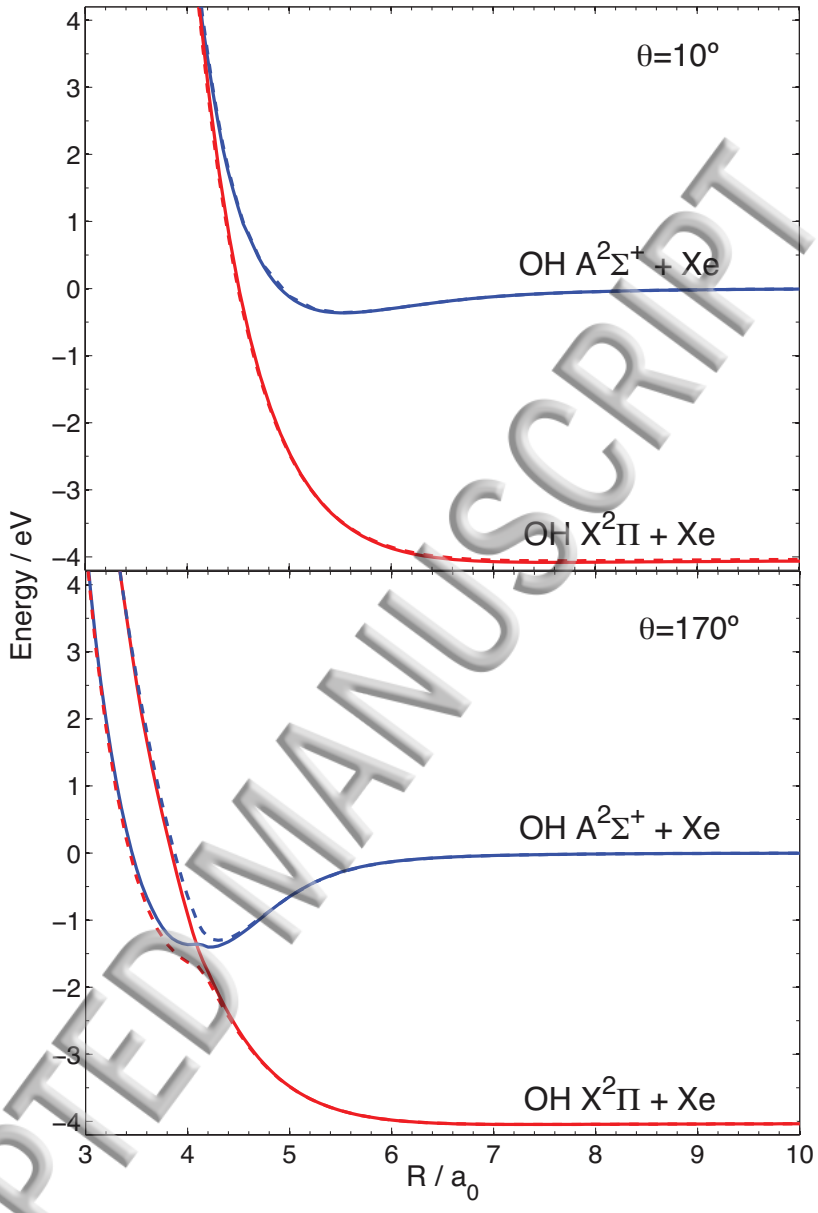


FIG. 1. The $H_{xx}$ (OH(X) + Xe, solid red line) and $H_{zz}$ (OH(A)+Xe, solid blue line) MRCISD+Q diabatic potential energy curves, relative to the OH(A)+Xe asymptote, are represented as a function of the Jacobi distance $R$ for the nearly collinear OH–Xe (top panel) and HO–Xe (bottom panel) geometries. The red and blue dashed lines show the $1A'$ and $2A'$ electronically adiabatic potential curves. The $1A'' = H_{yy}$ adiabatic curve practically overlaps with the $H_{xx}$ diabat and is not shown for clarity.

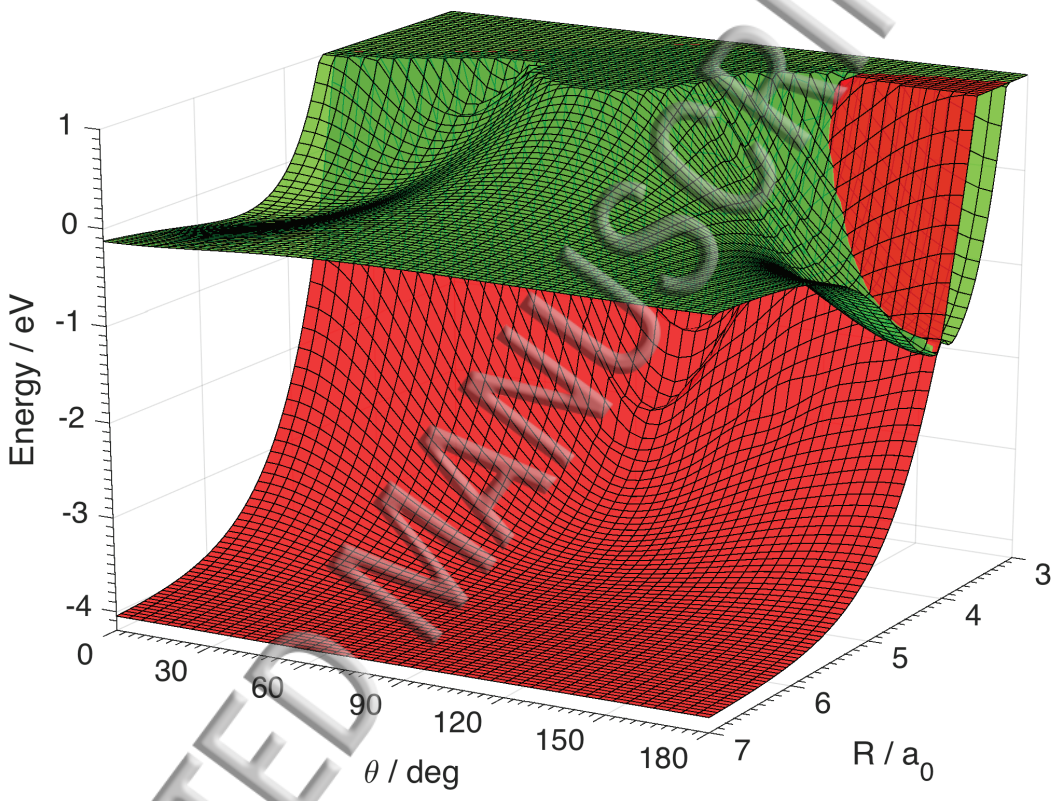


FIG. 2. Surface plots, relative to the OH $^2\Sigma^+$ +Xe asymptote, for the $H_{xx}$ (red, lower surface) and $H_{zz}$ (light green, upper surface) *diabatic* MRCISD+Q PESs as function of $(R, \theta)$ Jacobi coordinates. Values of $\theta = 0°$ and $\theta = 180°$ correspond to collinear O-H–Xe and H-O–Xe arrangements, respectively.

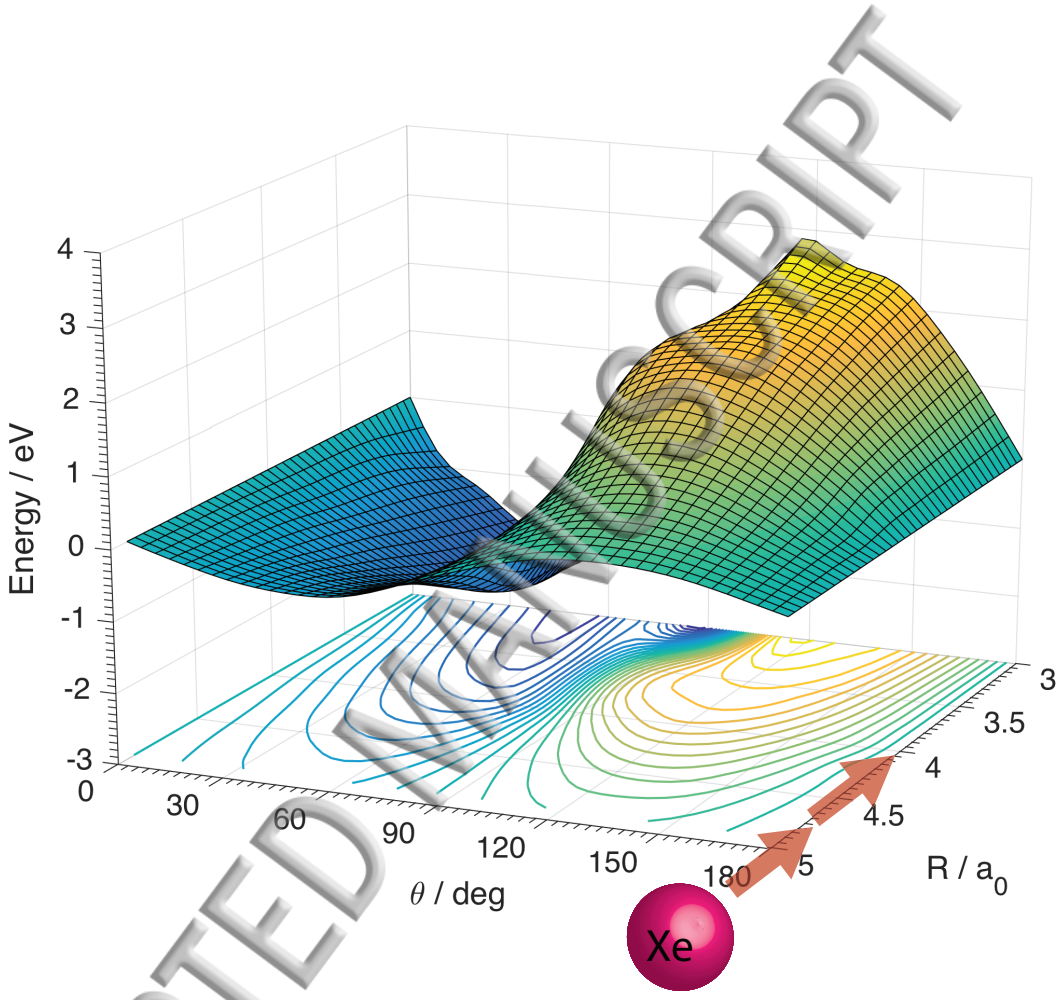


FIG. 3. Surface and contour plots representing the $H_{xz}$ diabatic coupling MRCISD+Q PES. The coupling vanishes at the collinear geometries and changes sign at a nearly perpendicular geometry. The sphere and arrows represent the approaching Xe atom to the region of the diabatic PESs where quenching process takes place in the vicinity of the Jacobi angle $\theta \in [140 - 180°]$, where the crossing between $H_{xx}$ and $H_{zz}$ diabats takes place, as shown in Fig. 2.

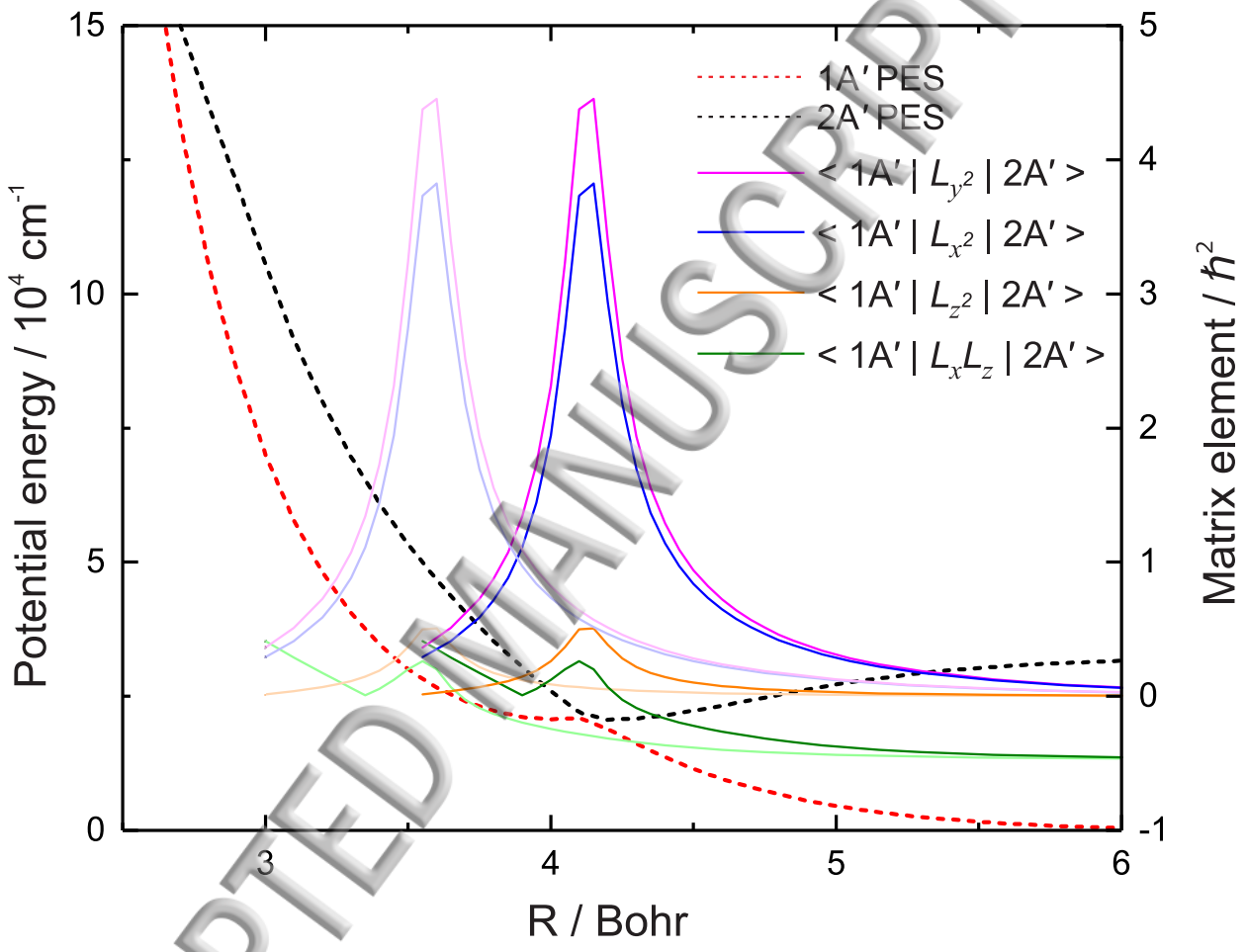


FIG. 4. Comparison of the $2A'$ and $1A'$ adiabatic PESs, and a selection of matrix elements that couple them, for the OH+Xe system, taken at a Jacobi angle of $\theta = 175°$. The matrix elements in bold color are the result of taking the faintly-colored elements for OH+Kr and shifting them in $R$.

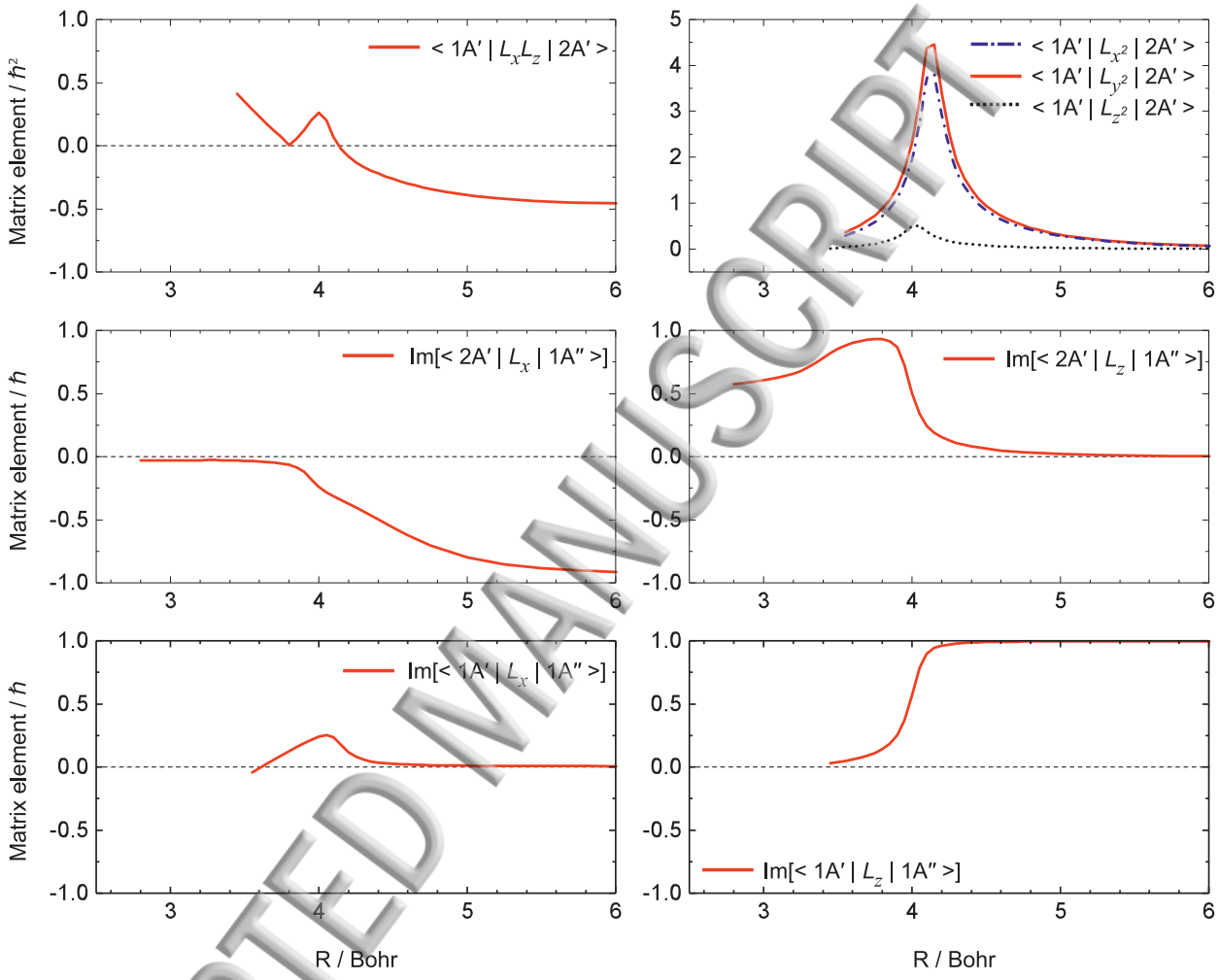


FIG. 5. Orbital electronic angular momentum matrix elements for OH+Xe in the near-linear Xe–O-H geometry ($\theta = 175°$) as a function of the Jacobi coordinate $R$. The matrix elements $\langle 2A'|L_x|1A''\rangle$ and $\langle 2A'|L_z|1A''\rangle$ have been specifically calculated for Xe+OH, while the remainder have been estimated from the corresponding elements for Kr+OH. The label 'Im' indicates that the imaginary part of the matrix element is plotted. Note the difference in the ordinate scales.

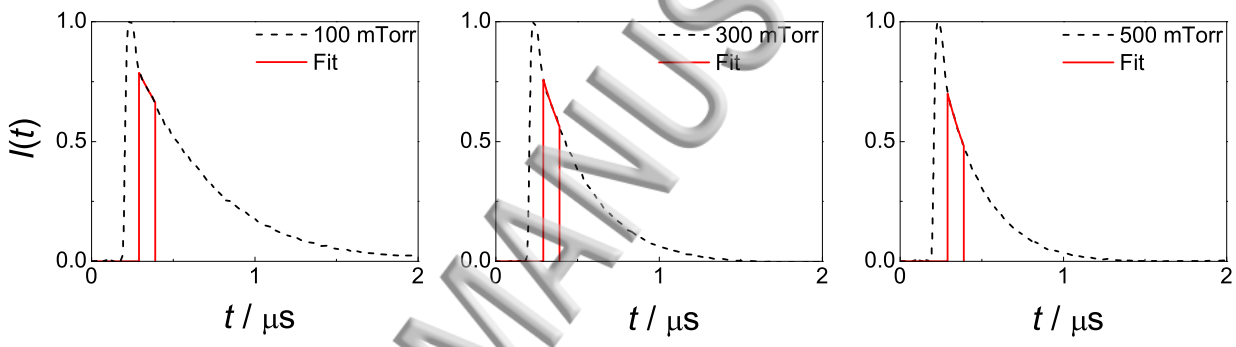


FIG. 6. Experimental, summed fluorescence decays for OH(A) + Xe, excited on the R branch to $N = 9$, $j = 8.5$. Black dashed lines: experimental data; red solid lines: exponential fit to first 100 ns after laser peak. Left: 100 mTorr Xe; center: 300 mTorr Xe; right: 500 mTorr Xe.

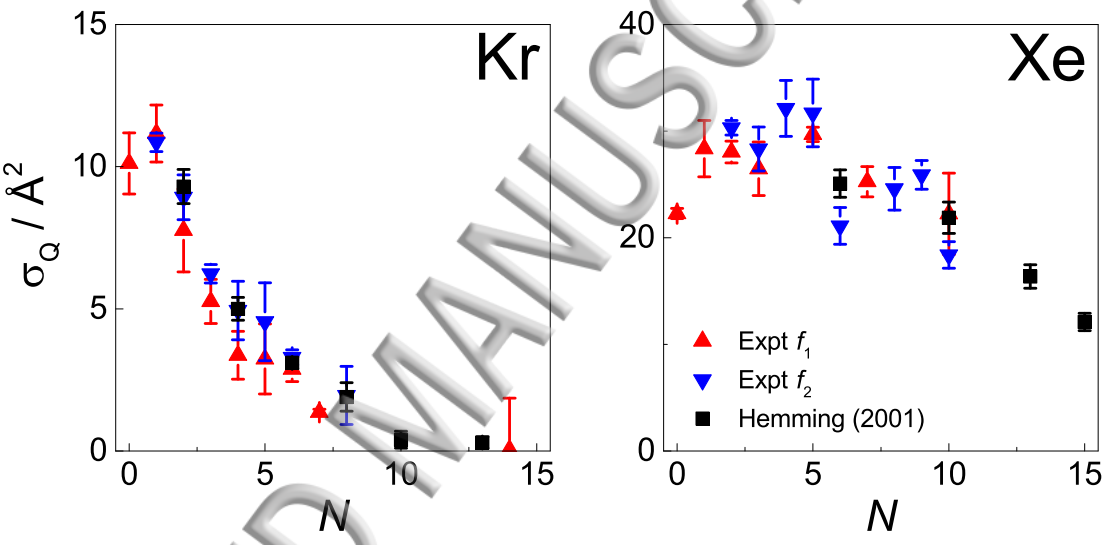


FIG. 7. Experimental electronic quenching cross-sections for OH(A) + Kr from Ref. 8 (left) and OH(A) + Xe (right). Red triangles: $f_1$, blue triangles: $f_2$, black squares: Hemming *et al* (Ref. 1. Note the difference in the ordinate scales.

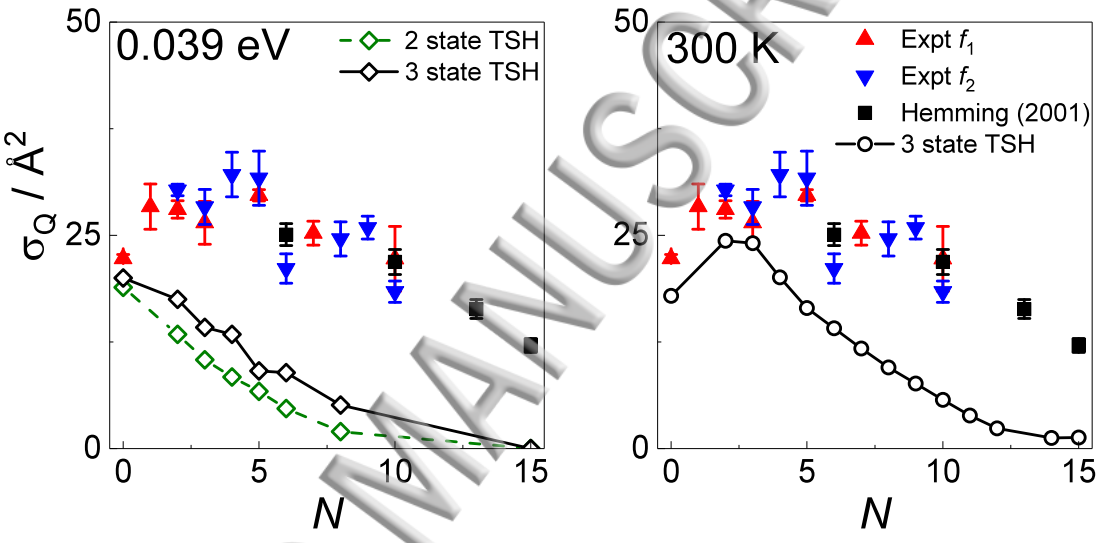


FIG. 8. Electronic quenching cross-sections for OH(A) + Xe. Red triangles: $f_1$ experimental; blue triangles: $f_2$ experimental; black squares: Hemming *et al.* experiments. Open symbols are theoretical data (green: two-state TSH-QCT; black: three-state TSH-QCT), using diamonds to represent fixed-collision-energy calculations (0.039 eV, left panel) and circles for calculations that sample a continuous collision energy range (300 K, right panel).

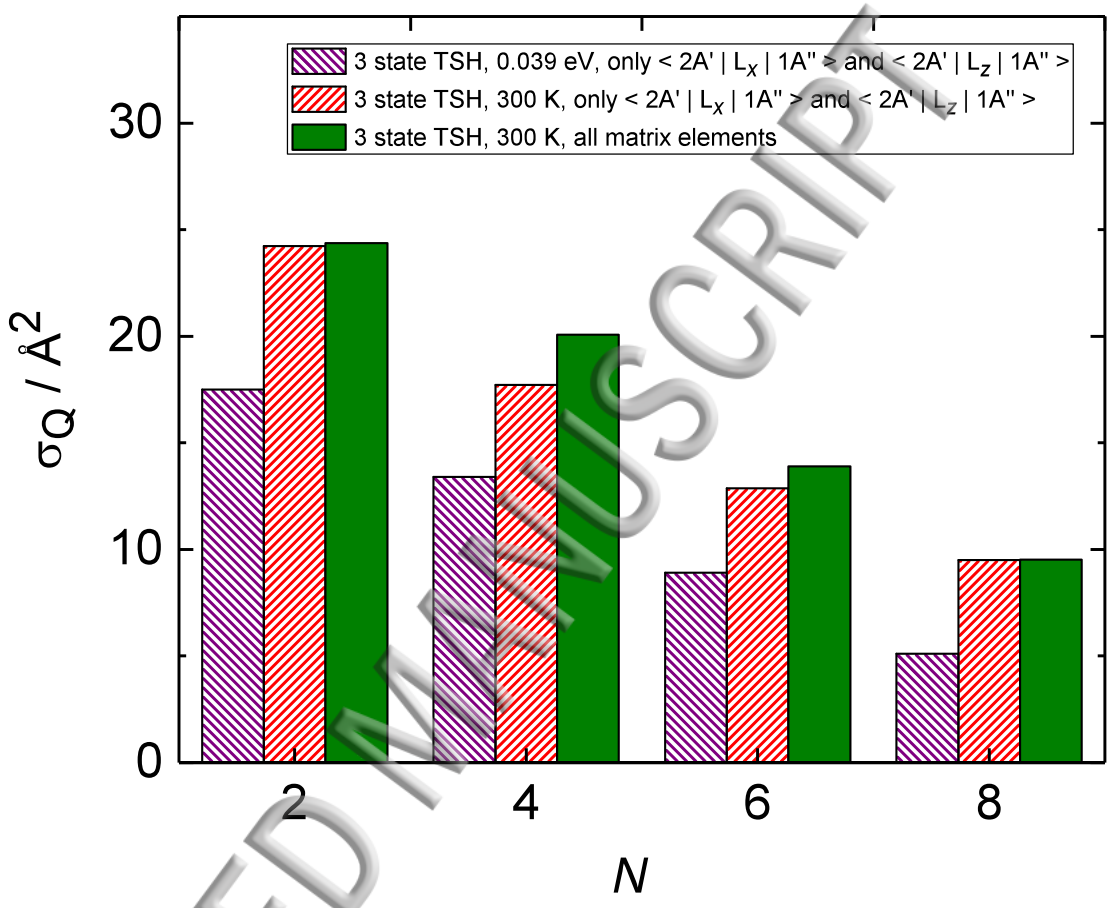


FIG. 9. Electronic quenching cross-sections for OH(A) + Xe. Data are shown from calculations that were run using: a fixed-collision-energy (0.039 eV), three-state model that included only the calculated ($\langle 2A'|L_x|1A''\rangle$ and $\langle 2A'|L_z|1A''\rangle$) roto-electronic coupling matrix elements (blue striped bars); a variable-collision-energy (300 K), three-state model that included only the calculated roto-electronic coupling matrix elements (red striped bars); and a variable-collision-energy (300 K), three-state model that included both the calculated roto-electronic coupling matrix elements and the remaining elements that were estimated from those of OH+Kr (solid green bars).

This manuscript was accepted by J. Chem. Phys. Click here to see the version of record.

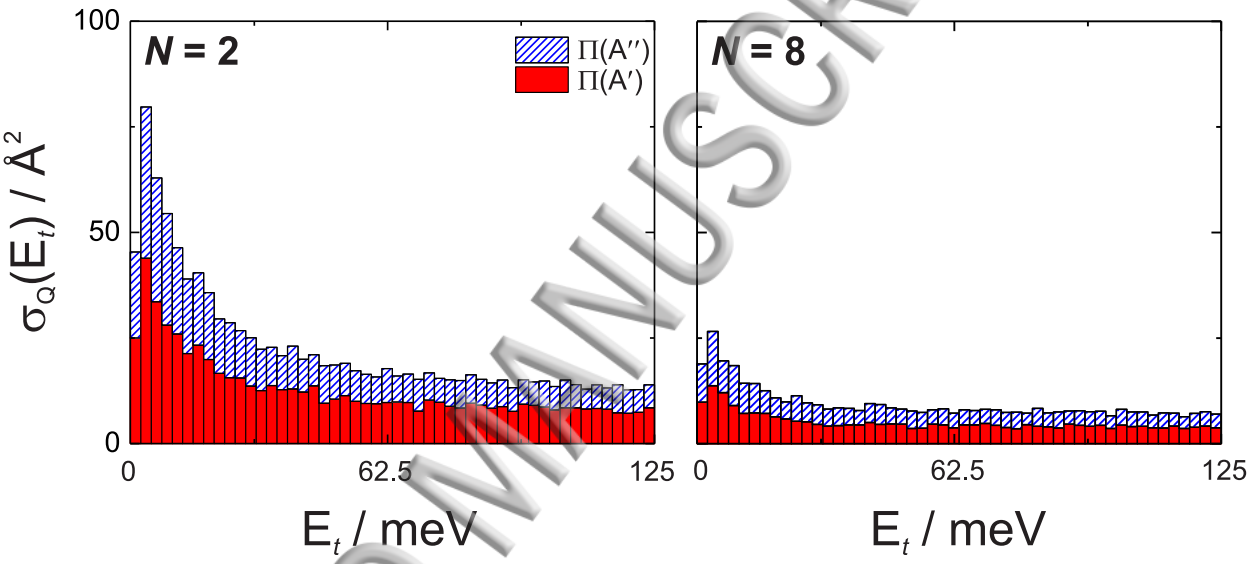


FIG. 10. Excitation functions (dependence of cross-section on collision energy) for electronic quenching of OH(A) + Xe, calculated using three-state TSH-QCT (300 K) summed over final $N''$ rotational states but resolved in the final Λ-doublet states. Left: initial $N = 2$. Right: initial $N = 8$.

This manuscript was accepted by J. Chem. Phys. Click here to see the version of record.

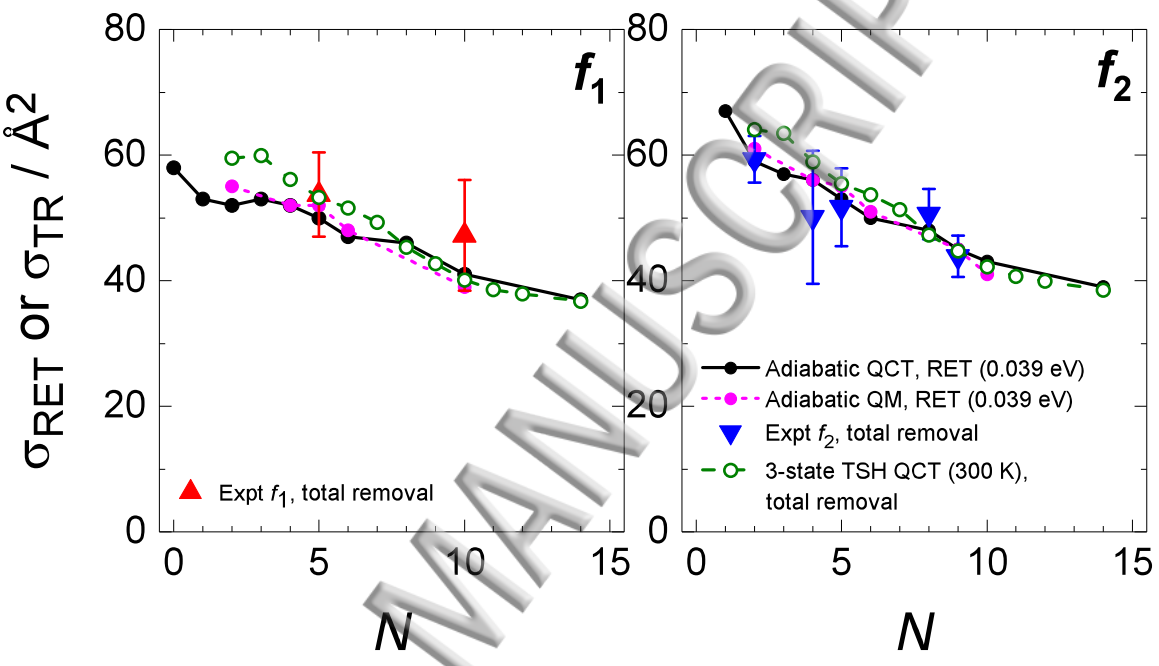


FIG. 11. Cross-sections for rotational energy transfer and *total removal* (sum of electronic quenching and RET cross-sections) for OH(A) + Xe. Left panel: from $f_1$ ($j = N + 1/2$) states (red triangles). Right panel: from $f_2$ ($j = N - 1/2$) states (blue triangles). Green open circles connected by dashed-line: three-state TSH-QCT calculations that sample a continuous range of collision energies (300 K). Black solid circles connected by a solid line: QCT adiabatic calculations on the $2A'$ PES. Magenta solid circles connected by a short-dashed line: QM calculations on the $2A'$ PES. Note that the last two calculations ignore the existence of quenching.

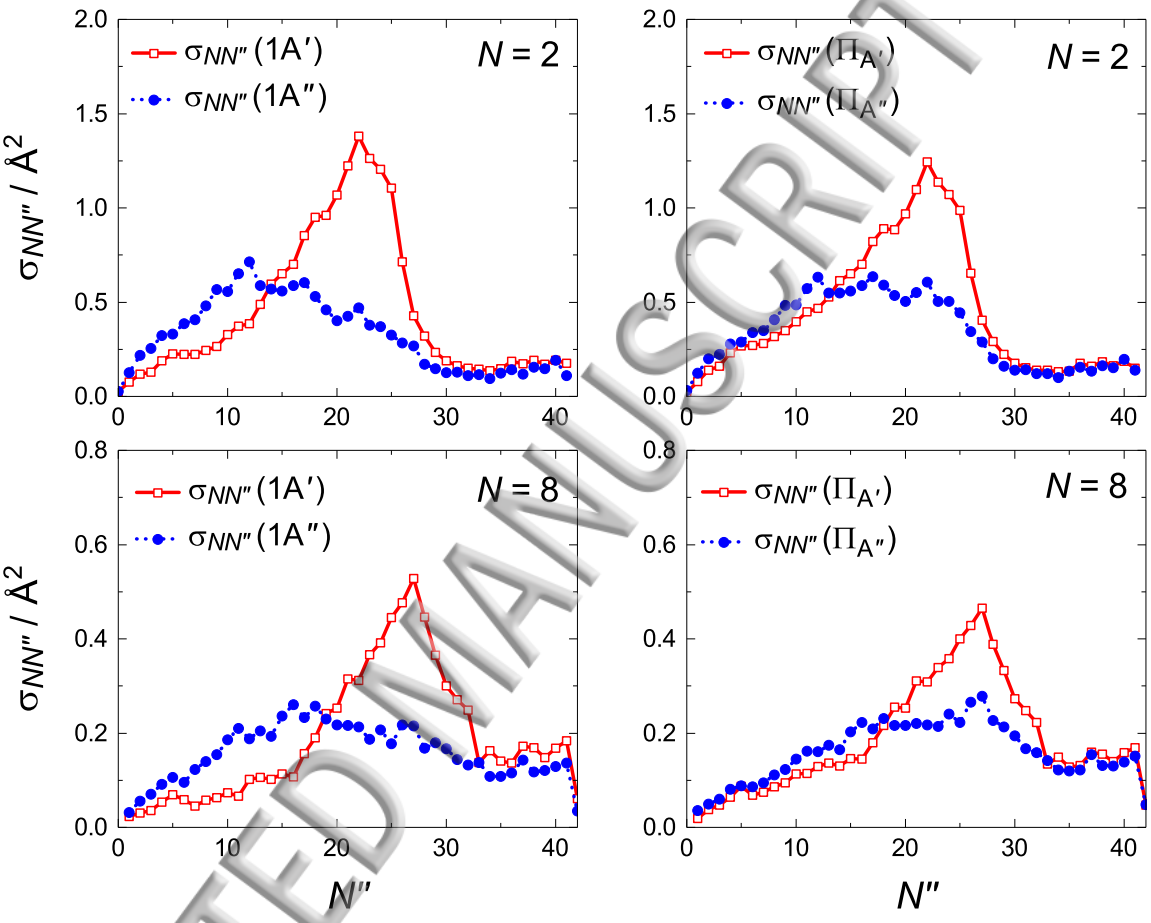


FIG. 12. Left panel: Product rotational-state distributions resulting from OH($A^2\Sigma^+$, $N$=2,8) + Xe → OH($X^2\Pi$, $N''$) + Xe transitions terminating on the $1A'$ (red) and $1A''$ (blue) PESs. Right panel: product rotational-state distributions for quenched OH(A)+Xe trajectories that began in the $N = 2$ and $N = 8$ initial rotational states of OH(A) and terminated in each of the ground-state Λ-doublets of OH(X).

This manuscript was accepted by J. Chem. Phys. Click here to see the version of record.

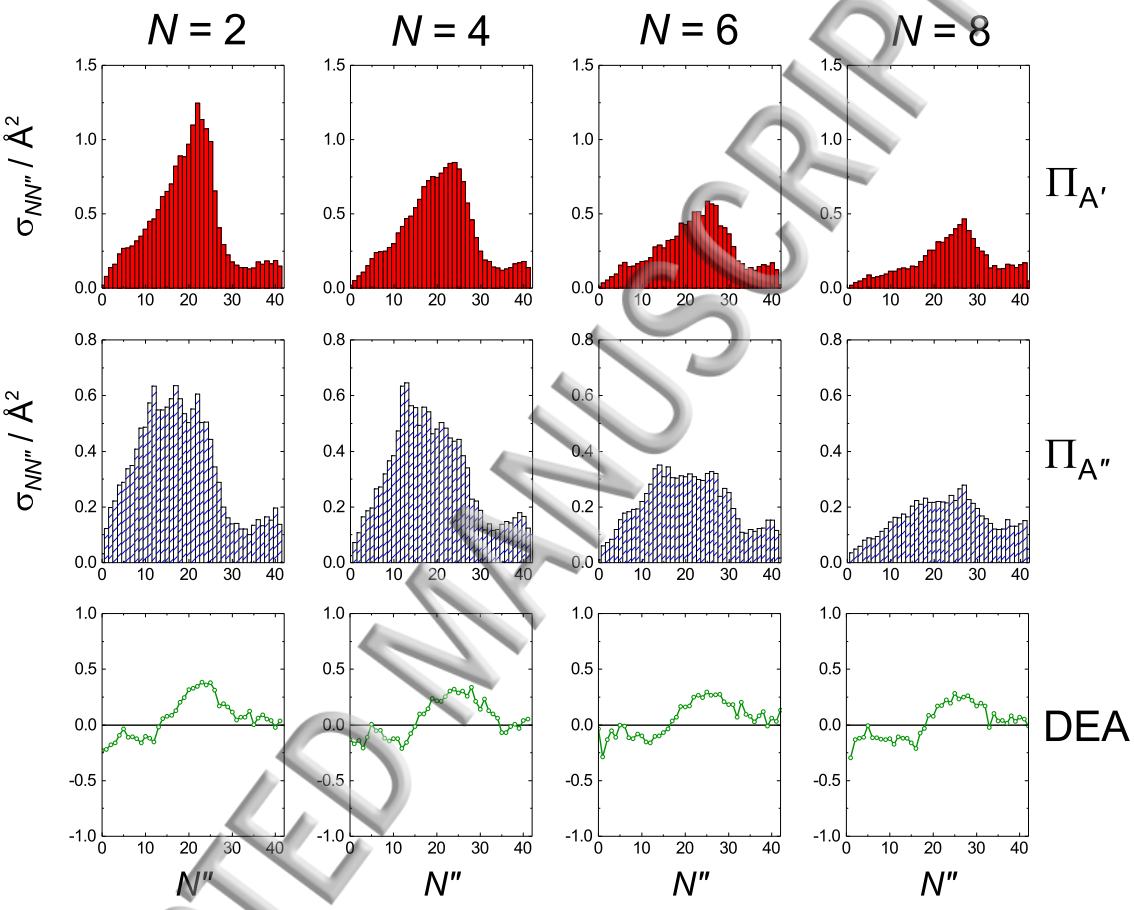


FIG. 13. Upper and middle panels: Theoretical rotational-state-resolved cross-sections, $\sigma_{NN''}$, for the non-adiabatic transfer of population for OH(A, $N$) + Xe $\rightarrow$ OH(X, $N''$) + Xe transitions. The cross-sections are further resolved in the terminal $\Lambda$-doublet ($\Pi_{A'}$ or $\Pi_{A''}$). Note the difference in the ordinate scales of the upper and middle panels. Lower panel: DEA for the same transitions.

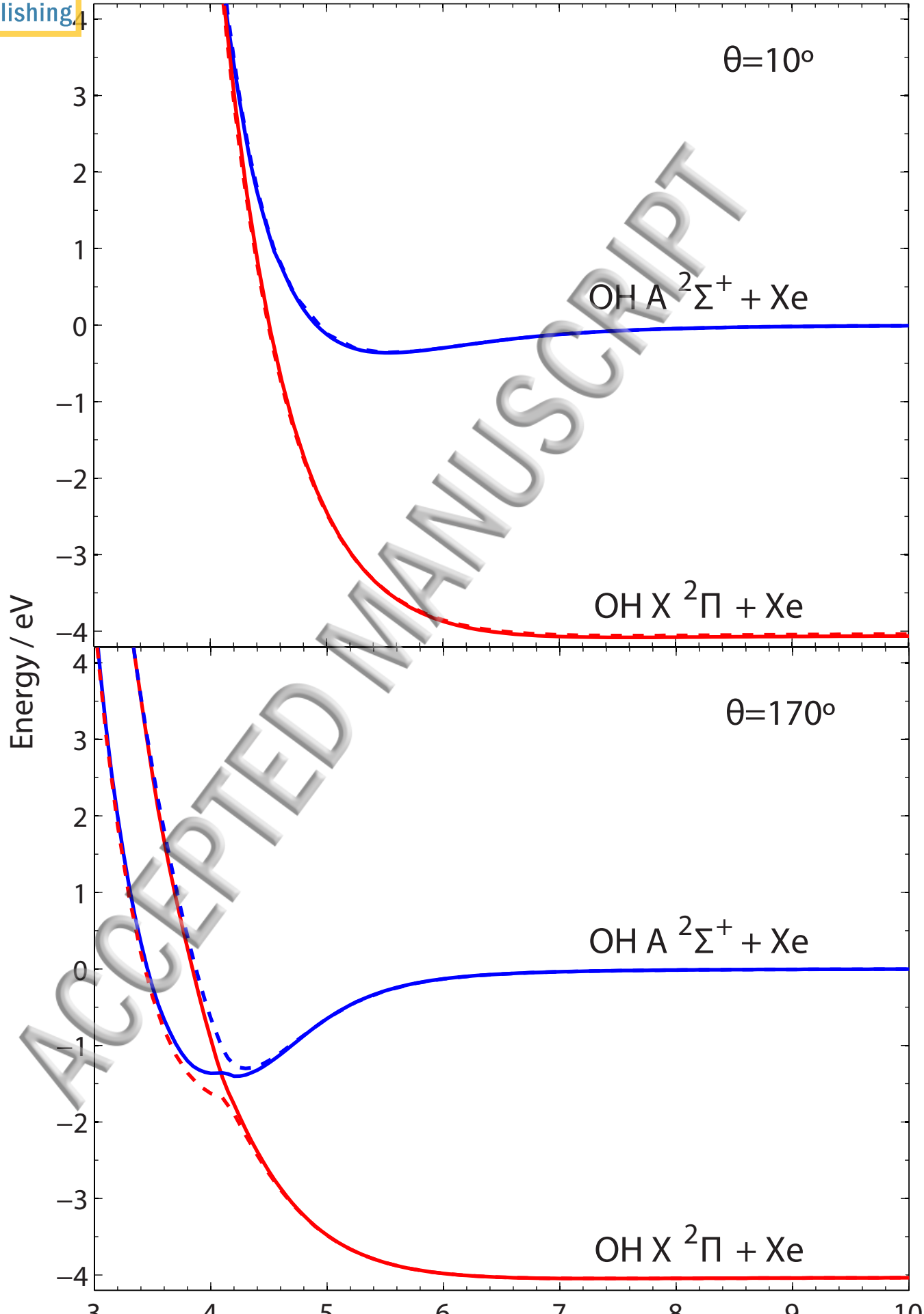

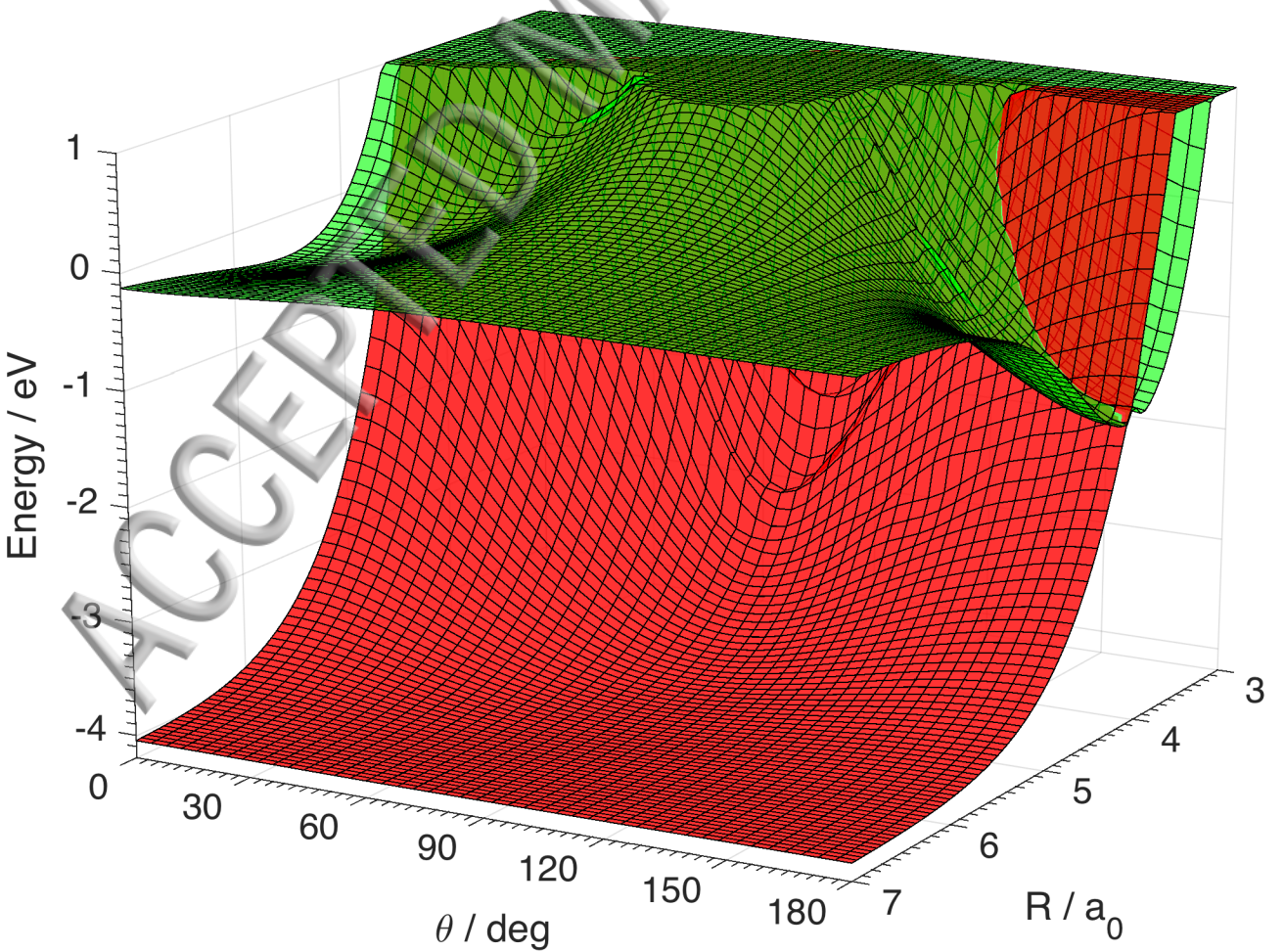

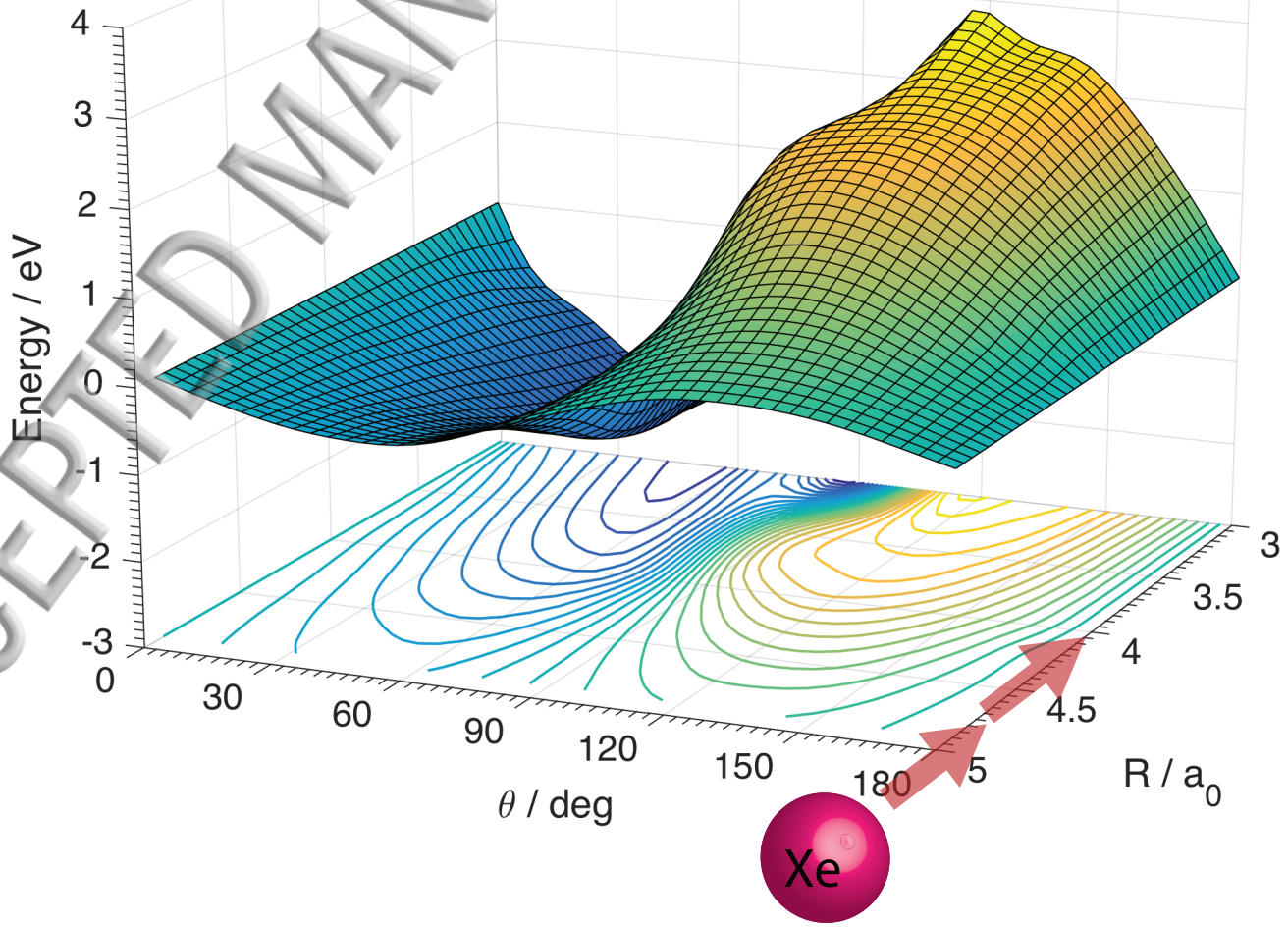

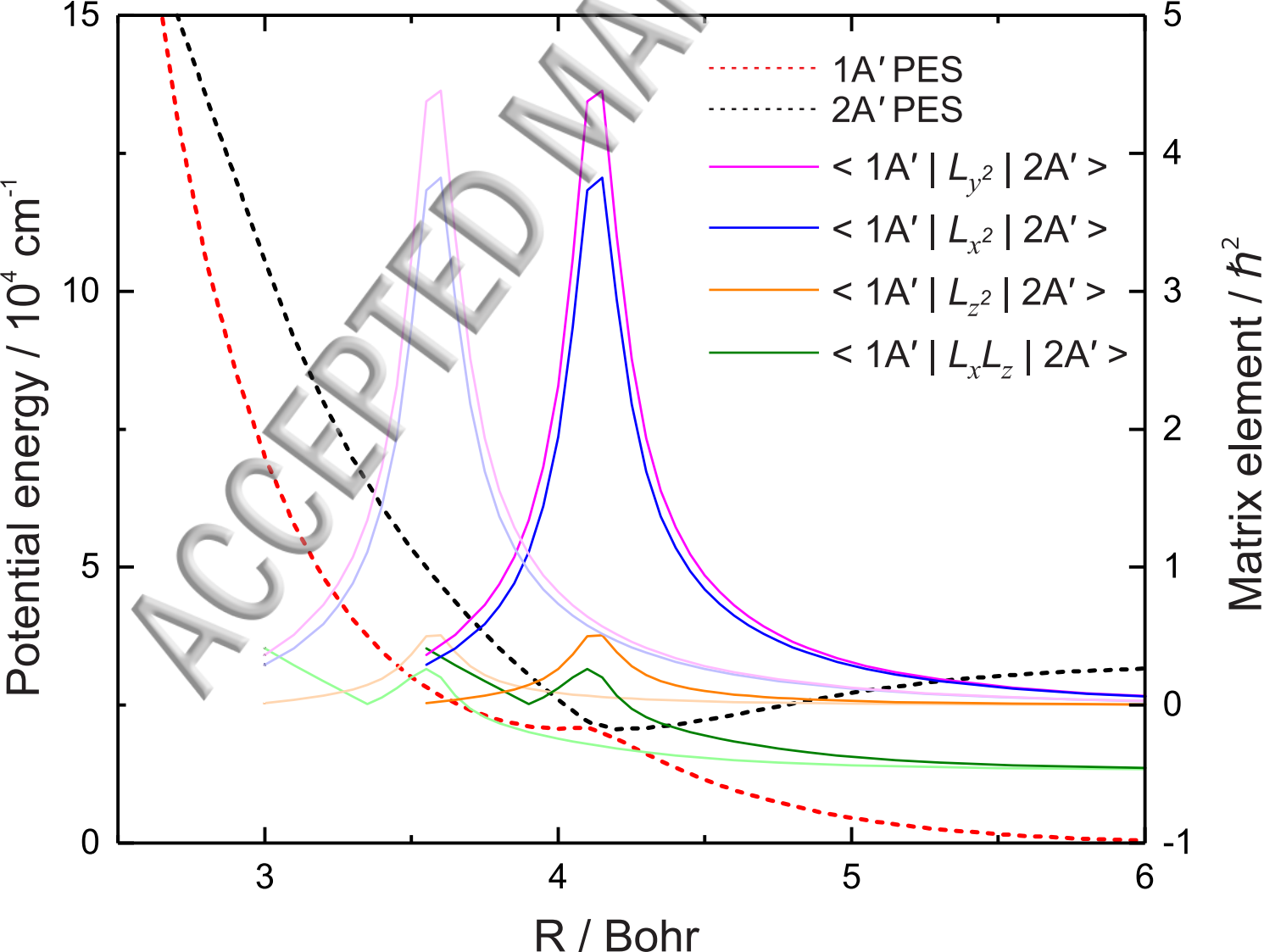
1A′ PES
2A′ PES
< 1A′ | $L_{y^2}$ | 2A′ >
< 1A′ | $L_{x^2}$ | 2A′ >
< 1A′ | $L_{z^2}$ | 2A′ >
< 1A′ | $L_xL_z$ | 2A′ >
Potential energy / $10^4$ cm$^{-1}$
Matrix element / $\hbar^2$
R / Bohr
0
5
10
15
-1
0
1
2
3
4
5
3
4
5
6

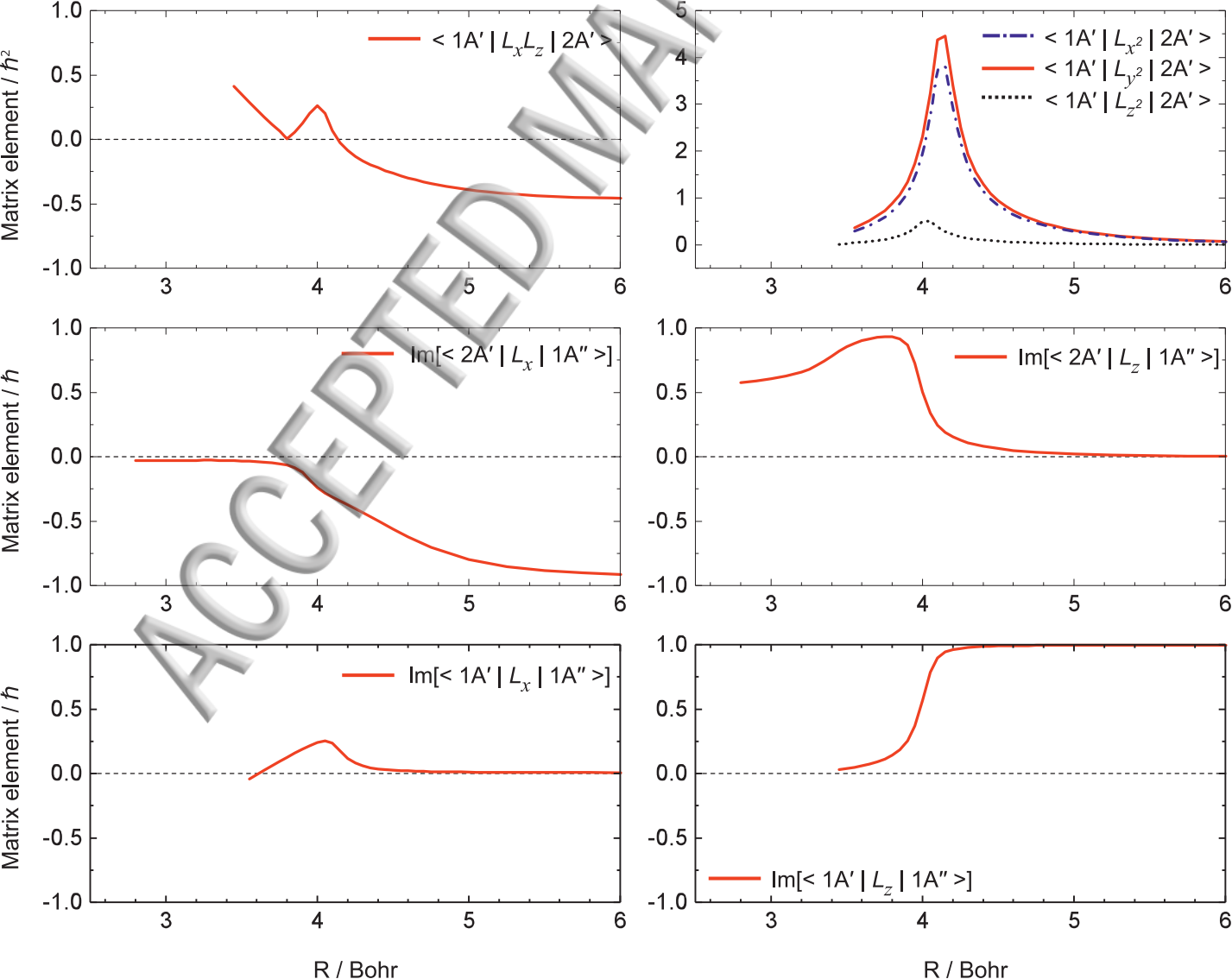

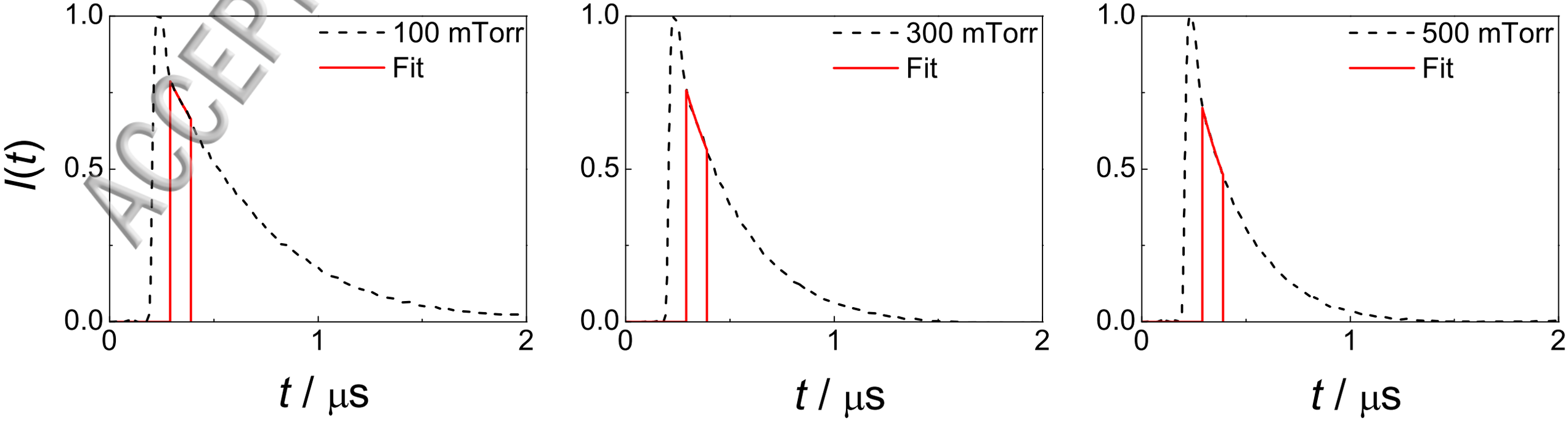
I(t)
1.0
0.5
0.0
0
1
2
t / μs
100 mTorr
Fit
300 mTorr
Fit
500 mTorr
Fit

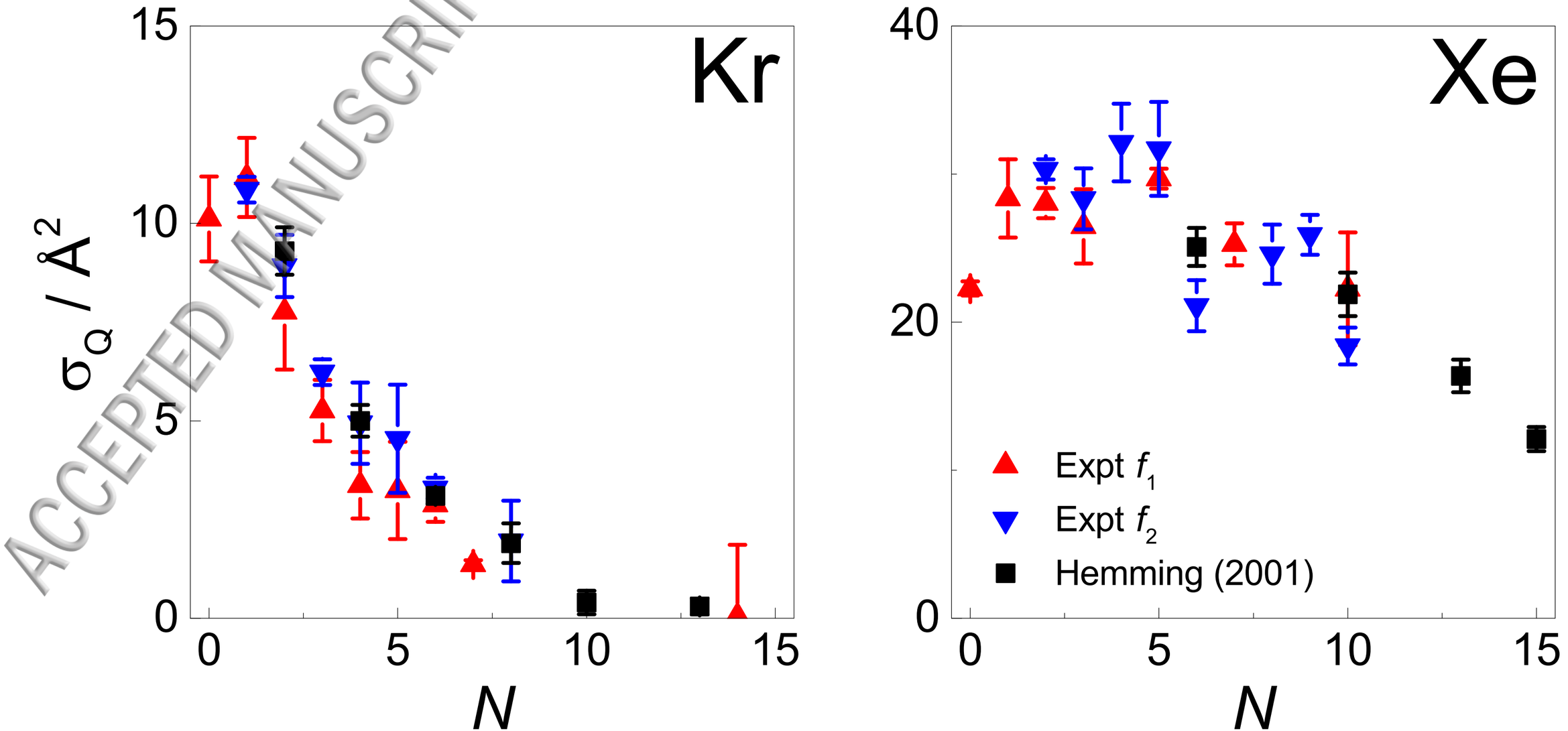

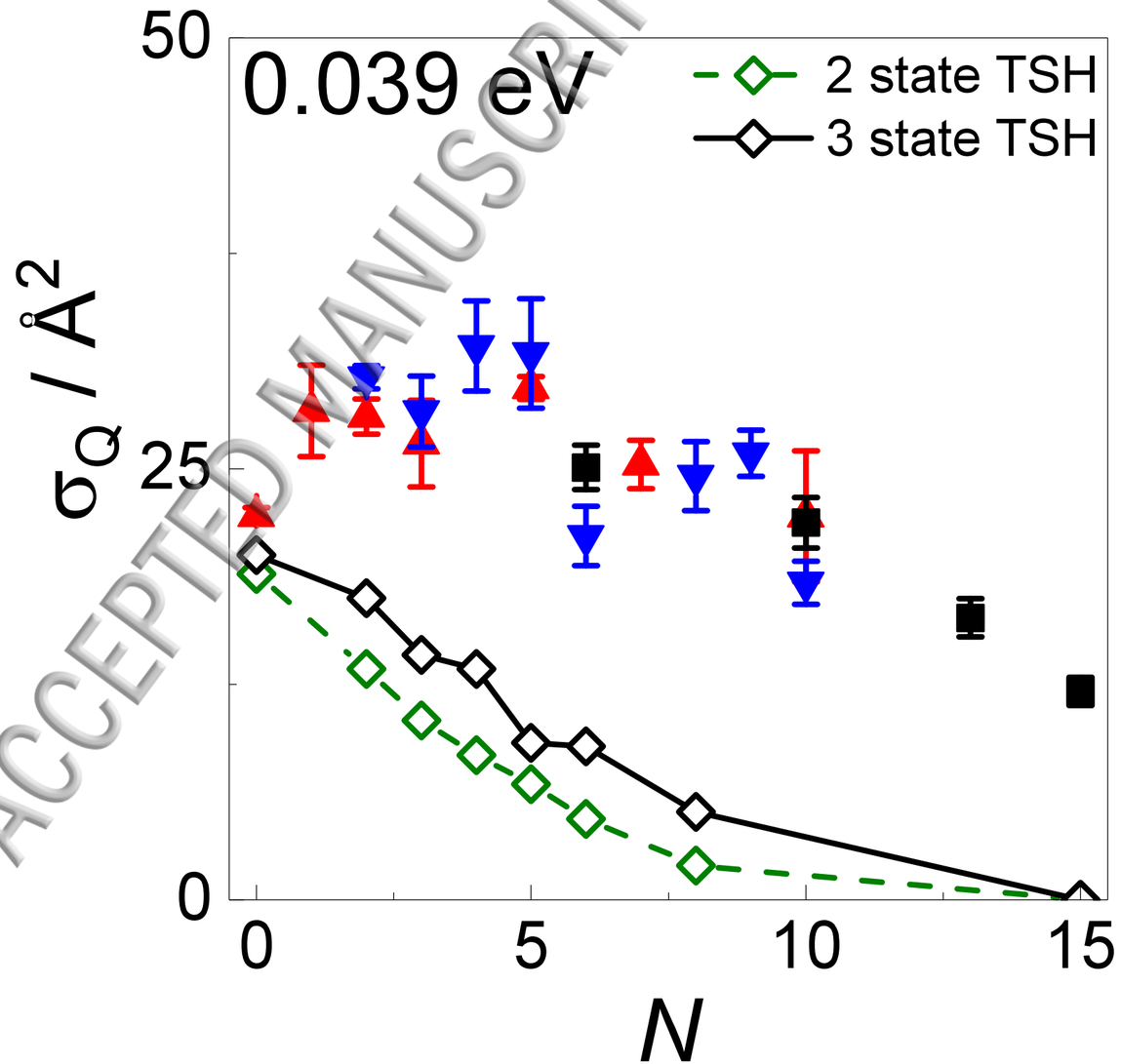


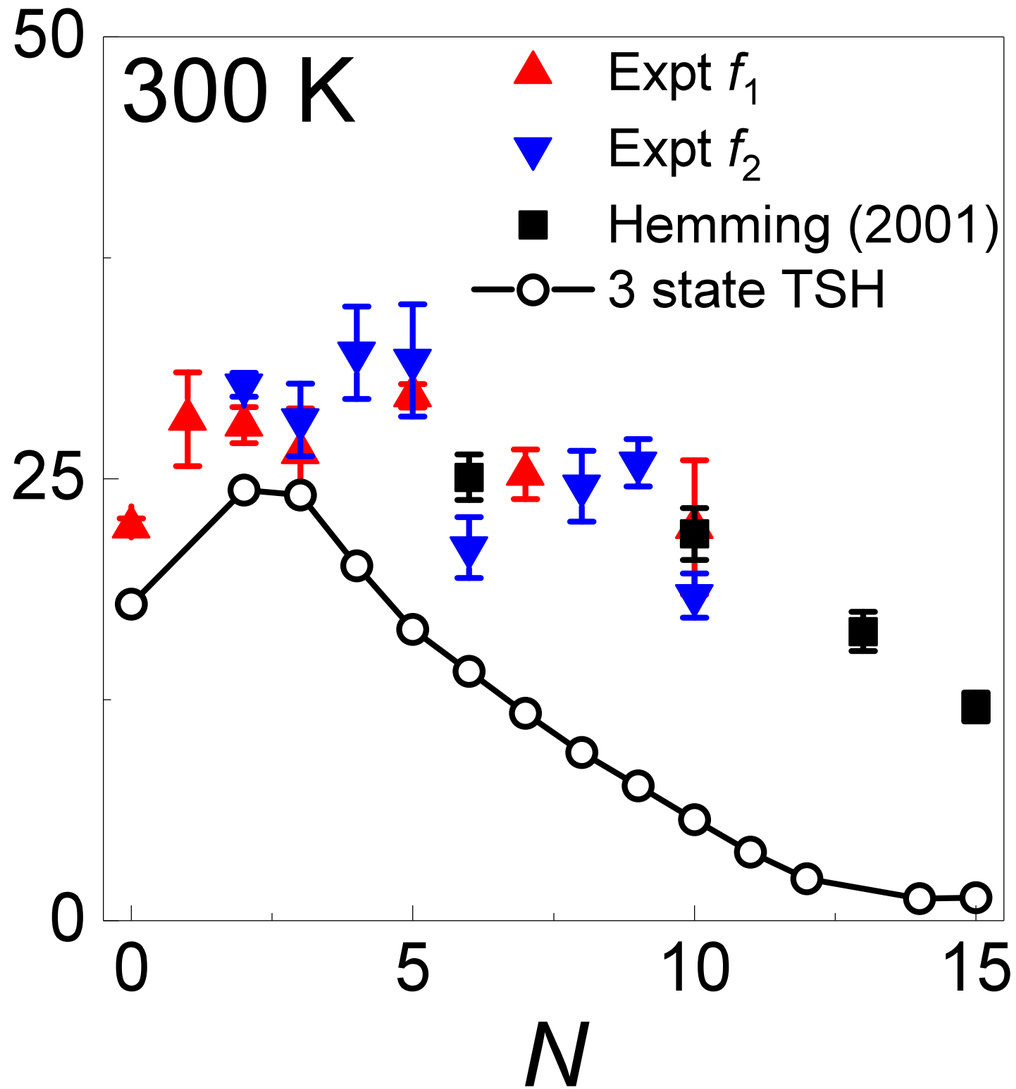

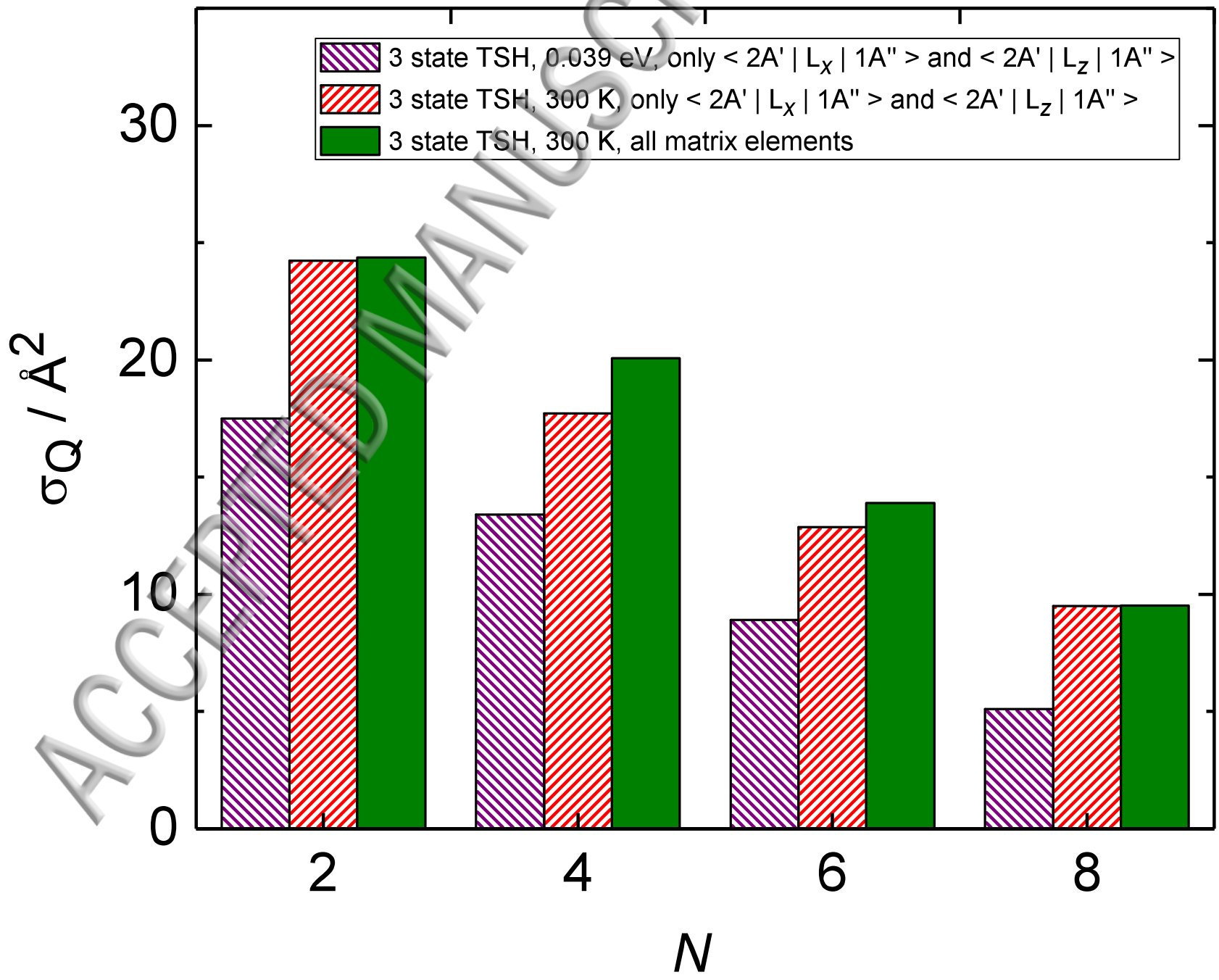

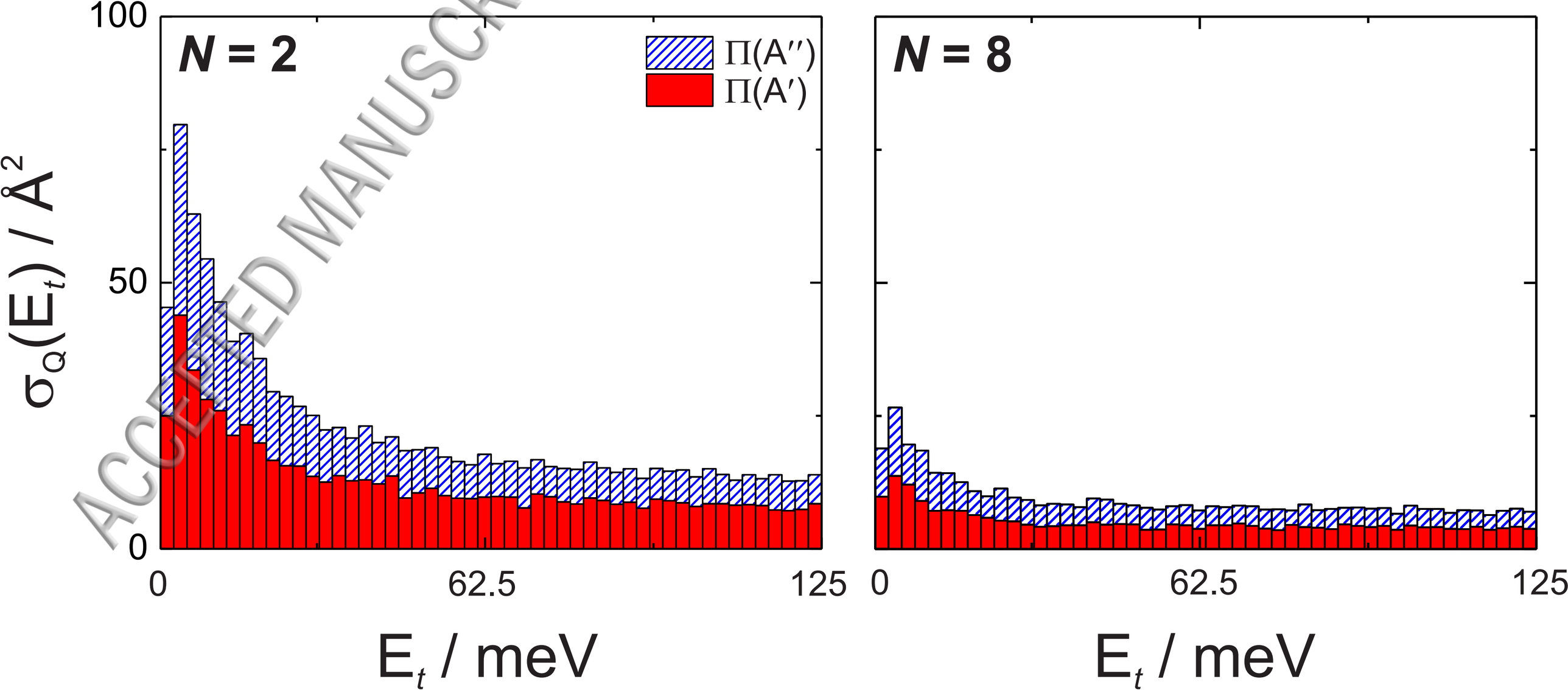

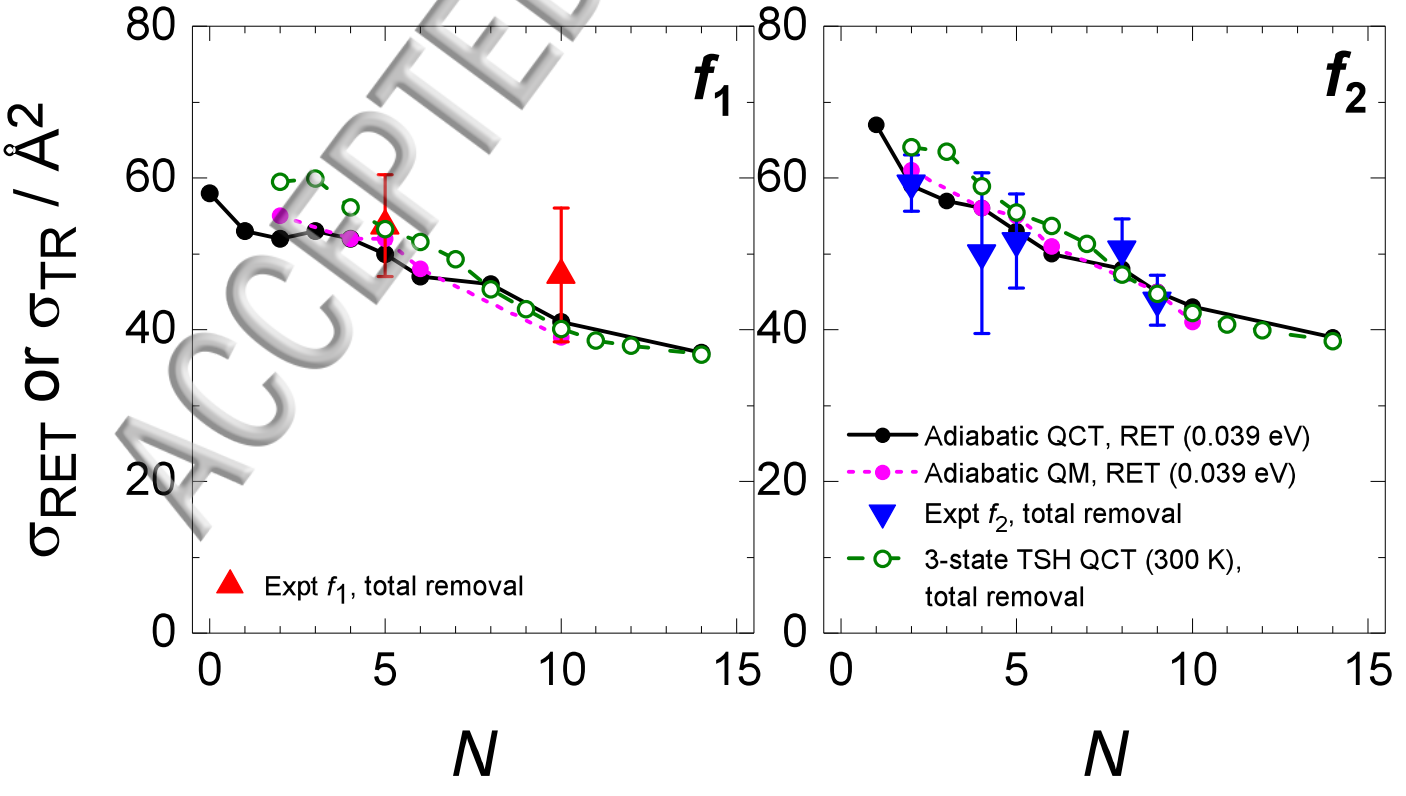
$\sigma_{RET}$ or $\sigma_{TR}$ / Å2
80
60
40
20
0
0
5
10
15
N
$f_1$
Expt $f_1$, total removal
$f_2$
Adiabatic QCT, RET (0.039 eV)
Adiabatic QM, RET (0.039 eV)
Expt $f_2$, total removal
3-state TSH QCT (300 K), total removal